

# Material-extrusion based additive manufacturing of BaTiO<sub>3</sub> ceramics: from filament production to sintered properties

Subhadip Bhandari<sup>a,b</sup>, Peter Veteška<sup>b</sup>, Gaurav Vajpayee<sup>c,d</sup>, Manuel Hinterstein<sup>c,d</sup>,  
Luboš Bača<sup>b,e</sup>, Zora Hajdúchová<sup>b</sup>, Zdenko Špitalský<sup>f</sup>, Giorgia Franchin<sup>a,\*</sup>, Marián Janek<sup>b,g,\*\*</sup>

<sup>a</sup> Department of Industrial Engineering, University of Padova, Via Marzolo 9, Padova 35131, Italy

<sup>b</sup> Department of Inorganic Materials, Faculty of Chemical and Food Technology, Slovak University of Technology in Bratislava, Radlinského 9, Bratislava 821 37, Slovakia

<sup>c</sup> Fraunhofer IWM, Freiburg 79108, Germany

<sup>d</sup> Institute of Applied Materials, Karlsruhe Institute of Technology, Karlsruhe 76131, Germany

<sup>e</sup> Aerospace and Advanced Composites GmbH, Wiener Neustadt A-2700, Austria

<sup>f</sup> Polymer Institute, Slovak Academy of Sciences, Dúbravská cesta 9, Bratislava 845 41, Slovakia

<sup>g</sup> Department of Physical and Theoretical Chemistry, Faculty of Natural Sciences, Comenius University, Mlynská dolina, Ilkovičova 6, CH1, Bratislava SK-84215, Slovakia

## ARTICLE INFO

### Keywords:

Material extrusion  
BaTiO<sub>3</sub>  
Debinding  
Sintering  
Dielectric  
Ferroelectric

## ABSTRACT

Material extrusion (MEX) of thermoplastic filaments represents one of the most widely adopted additive manufacturing (AM) technologies. Unlike vat photopolymerization and powder-bed fusion methods that require high energy sources such as UV light and lasers, this fabrication method can be adapted for the fabrication of ceramics by using ceramic loaded filaments as feedstock, yet still employing relatively cheap equipment meant for polymeric materials with little adaptation of the process parameters; this potentially enables a broader diffusion of AM ceramic components. In this work, composite filaments with various weight fractions (60 – 80 wt %) of BaTiO<sub>3</sub> were fabricated and characterized by electron microscopy, compressive mechanical testing, rheometry and thermogravimetric analysis to ensure a smooth and reliable printing process. After optimizing the printing parameters, the dense and porous printed samples were carefully debinded and sintered to obtain dense (~ 92 %) and defect-free ceramic bodies. The sintered samples were characterized for phase development, microstructure, and pore size distribution. Careful observations reveal a particular range of pore size (0.1 – 5 μm), which originates from the binder burn out process. The dielectric and ferroelectric properties of the fabricated samples were in good agreement with those reported in previous literature. This work provides a foundation for rapid prototyping of functional electro ceramics into reliable products with desired functional properties.

## 1. Introduction

In recent years, there has been an increasing interest in piezoelectric ceramics due to their ability to transform mechanical stimuli into electrical energy or vice versa [1]. Leading this family of materials is lead zirconate titanate (PZT), extensively used in energy harvesting, sensors, actuators, etc. due to its exceptionally high electrical properties [2,3]. However, the presence of highly toxic lead (Pb) poses an environmental and health hazard and therefore restricts the application and further

development of PZT devices [4,5]. Therefore, environmentally friendly lead-free piezoelectric compositions have been investigated and barium titanate (BaTiO<sub>3</sub>) has emerged as a viable solution [6].

A wide range of conventional ceramic processing technologies such as slip casting [7], tape casting [8], die pressing [9], injection molding [10], micro-extrusion [11] etc. have been utilized to fabricate BaTiO<sub>3</sub> piezoceramics. However, there are still certain limitations associated with these conventional techniques, particularly when complex geometries are sought: these include time-consuming manufacturing

\* Corresponding author.

\*\* Corresponding author at: Department of Inorganic Materials, Faculty of Chemical and Food Technology, Slovak University of Technology in Bratislava, Radlinského 9, Bratislava, Slovakia.

E-mail addresses: [giorgia.franchin@unipd.it](mailto:giorgia.franchin@unipd.it) (G. Franchin), [marian.janek@stuba.sk](mailto:marian.janek@stuba.sk) (M. Janek).

<https://doi.org/10.1016/j.addma.2024.104238>

Received 12 January 2024; Received in revised form 16 April 2024; Accepted 29 May 2024

Available online 31 May 2024

2214-8604/© 2024 The Author(s). Published by Elsevier B.V. This is an open access article under the CC BY-NC-ND license (<http://creativecommons.org/licenses/by-nc-nd/4.0/>).

processes with high labor costs and extremely high rates of wear of the expensive machining tools utilized [12]. Furthermore, the mechanical stress applied during the machining process of the sintered samples often leads to grain pull out, compromising the surface finish [13]. Consequently, this deterioration significantly impacts the overall performance of the piezoelectric component. A possible solution to these problems came with the evolution of innovative additive manufacturing (AM) technologies that enable the manufacture of complex ceramic structures that were not achievable by conventional means with high accuracy.

Despite the fact that ceramic additive manufacturing is currently far behind metal and polymer AM in terms of technological advancement, the sector has made significant strides over the past three decades [12, 14,15]. A comprehensive review of additively manufactured piezoelectric ceramics has been reported by Chen et al. [1]. This review reveals that BaTiO<sub>3</sub> and BaTiO<sub>3</sub>-based ceramics have been studied with commercially available AM methods such as stereolithography (SLA), binder jetting (BJ), material extrusion (MEX), selective laser sintering (SLS), etc. In fact, the AM technologies have been modified in some other way to deal with ceramic materials, but each process has its own limitations.

For example, powder bed fusion techniques, such as selective laser melting (SLM), selective laser sintering (SLS), and directed energy deposition (DED), which are most commonly employed for metals and polymers, are generally not suitable for fabricating ceramics [12,16,17]. This is primarily due to the fact that ceramics require extremely high sintering temperatures, which exceed the capabilities of these processes. Moreover, the rapid laser heating and cooling involved in these techniques can lead to thermal shock, resulting in destruction or cracking of the intended ceramic parts [15]. Components fabricated using binder jetting are relatively porous (sintered density is usually less than 70 %) and result in an uneven or rough surface finish [14,18]. In addition, the flowability of fine ceramic particles is one of the main concerns that increases an additional step in the preparation of the starting powder [12]. Therefore, this technology is typically used specifically when porous structures are desired in applications such as biological scaffolds or implants. The latter uses a binder, while the former uses intensive laser energy for achieving the desired shape.

Vat photopolymerization (VPP), including stereolithography and digital light processing, relies on the curing capability of the photopolymeric resin in which the ceramic particles are dispersed. The presence of dark or gray ceramic powders such as SiC, Si<sub>3</sub>N<sub>4</sub>, or high refractive index powders such as BaTiO<sub>3</sub> can be challenging due to the absorption or scattering of UV light, respectively [19–21]. These phenomena can result in a poor surface finish, incomplete curing, and reduced resolution of the printed object. In addition, producing very large components is challenging due to the limited build volume area and the delicate debinding step.

All the aforementioned methods often require more expensive equipment compared to those used for polymers or extensive feedstock adjustment, which limits their use to mostly research and internal development. Material extrusion (MEX) methods, such as fused filament fabrication (FFF) or direct ink writing (DIW), provide a viable alternative with low equipment cost and high feedstock flexibility [12,14,15]. However, they also present a lower resolution (limited by the nozzle size and the material flow behavior) and higher surface roughness, when compared to other AM technologies such as VPP. In a typical FFF process for ceramics (also known as fused deposition of ceramics, FDC), the feedstock is usually in the form of composite filaments (thermoplastic polymer loaded with ceramic particles); the filament is heated to a molten state and then extruded through a fine nozzle on the print bed, where it solidifies to produce the desired shape. The part then undergoes debinding (i.e., removal of the organics) and sintering. In order to achieve high density in the sintered stage, the composite filaments must be heavily loaded with ceramic powder; this results in a steep increase in stiffness, yet some flexibility must be retained, as well as low viscosity

after melting [22]. In principle, the extrusion mechanism is very similar to Direct Ink Writing (DIW), which uses a ceramic paste instead of a filament as a feedstock. Energy savings (no need to heat the paste to extrude it) and low organic content are two major benefits of using DIW. However, the rheological behavior of the paste is very crucial and determines the success or failure of the printing process [23]. The solid loading and the addition of different additives have to be carefully tailored to produce a shear-thinning behavior during extrusion and allow for shape retention. Unsupported parts and overhangs are more limited than what can be achieved via FFF.

The simplicity in the FFF process lies in the fact that most of the commercially available thermoplastic polymers, such as polylactic acid (PLA), polycarbonate (PC), ethylene vinyl acetate (EVA), acrylonitrile-butadiene-styrene (ABS), nylon (PA), polyethylene (PE), polyvinylidene fluoride (PVDF), etc. can be used as a matrix to disperse the ceramic powder [24–32]. The thermoplastic binder and the ceramic powder should exhibit good compatibility to ensure homogeneity and avoid phase separation during mixing [33,34]. During the last decade, a wide variety of ceramic materials including zirconia [24,34], alumina [35,36], PZT [37], mullite [38], B<sub>4</sub>C [39], hydroxyapatite [40], and BaTiO<sub>3</sub> [25–31,37] have been used to produce composite filaments for FFF. Increasing the ceramic loading in the filament reduces the shrinkage and the probability of defects being generated. However, sufficient flexibility and strength are also needed for the filaments to be spooled for storage and to ensure smooth de-spooling during the printing process, while highly loaded filaments tend to become quite brittle and often break in the feeder [41]. Moreover, high ceramic loadings complicate the feedstock production process, as particles tend to agglomerate and produce inhomogeneous filaments. In addition, the viscosity of the composite mixture at the printing temperature should be low enough to ensure smooth and consistent flow; however, with highly filled ceramic powder, this is quite challenging, as the particles tend to increase the viscosity and clog the nozzle, resulting in inconsistent flow of material and printing flaws [42]. Khatri et al. produced BaTiO<sub>3</sub>-ABS filaments, ensuring consistent printing by incorporating up to 35 vol% BaTiO<sub>3</sub> powder into the polymer matrix; increasing the filler ratio led to breakage at the print head and dimensional inaccuracies [31].

Furthermore, most of the investigations published to date on FFF of BaTiO<sub>3</sub> have only considered the use of printed components without further postprocessing, i.e., without the removal of the polymer matrix and the sintering of the ceramic powder [25–31]. During debinding, the onset of defects or distortions in the structure might occur; the choice of the polymeric matrix can strongly influence the outcome of the debinding process [43]. Sebastian et al. proceeded through the debinding and sintering 3D printed scaffold structures produced from a filament embedding 52 vol% of BaTiO<sub>3</sub> in EVA matrix [37]; however, the filament production and microstructural properties of the sintered scaffolds were only briefly addressed in the study.

At present, there has not yet been a comprehensive investigation on the production of FFF filaments tailored to produce sintered BaTiO<sub>3</sub> components, which creates an opportunity for further exploration. This research work is hence focused on the fabrication of composite filaments with different ceramic fractions, suitable for any open source FFF printer. A systematic study was conducted on the fabricated filaments to correlate their characteristics and performance. This includes thermal analysis, mechanical characterization, rheological behavior, and printability of the filaments. Furthermore, debinding and sintering parameters were carefully designed to obtain defect free, highly dense ceramic bodies, which were further characterized for dielectric and piezoelectric properties. The rigorous investigation into the parameters influencing filament quality, uniformity, and performance will allow to fine-tune production methods and increase the repeatability of FFF printing processes.

## 2. Materials and methods

### 2.1. Powder characterization

A commercial BaTiO<sub>3</sub> powder (JINAN Future Chemical co., ltd, China, Lot No. 221108) was used to manufacture the filaments with various ceramic loadings for the FFF process. The morphology, particle size distribution (PSD), X-ray diffraction (XRD) pattern, and inductively coupled plasma (ICP) analysis of the starting powders are reported in Fig. S1.

The theoretical density of the powder, measured with the He pycnometer, was  $5.84 \pm 0.01 \text{ g cm}^{-3}$ . *In situ* measurements of shrinkage of the ceramic powder used in composite manufacture was recorded using a heating microscope (Leica, Germany) and an M16 furnace fitted with a camera (Canon, USA) EOS700D (refer to Fig. S2). The powder was pressed into a 3 mm diameter disc and placed on a corundum sample holder. The sample holder was illuminated by background illumination (tungsten lamp) with a light temperature of approximately 2000 K and heated to 1400 °C using a heating rate of  $10 \text{ °C min}^{-1}$ .

### 2.2. Filament fabrication

To ensure the production of homogeneous composite filaments, a two-stage extrusion process was adopted. This approach was essential to prevent nozzle clogging caused by non-dispersed BaTiO<sub>3</sub> particles in the binder blend. Utilizing a twin-screw extruder type LTE 16-52 (Labtech Engineering Co., Ltd, Thailand), equipped with segmented screws of 16 mm in diameter and designed with two intense mixing zones, effective dispersion of the BaTiO<sub>3</sub> powder in the thermoplastic matrix was achieved. Prior to the initial extrusion, the BaTiO<sub>3</sub> powder and the biodegradable thermoplastic polymers, polyvinyl alcohol (PVA, binder A), and polycaprolactone (PCL, binder B), were subjected to a 24-hour drying process at 60 °C to reduce moisture content in the initial feedstock. A polymer blend ratio PVA:PCL = 3:2 was selected. The schematic depicting the process from filament production to the printing and sintering of the ceramic parts is displayed in Fig. 1.

The filament resulting from the first extrusion was chopped into granulate, and a second stage of filament extrusion was performed. This involved employing the necessary gauge and draw-off mechanism to

ensure precise control of the filament diameter at  $1.75 \pm 0.05 \text{ mm}$ . The typical average production mass rate of the composite filament was approximately  $1.2 \text{ kg h}^{-1}$  (filament speed  $50 \text{ cm min}^{-1}$ ) during the first extrusion and around  $0.5 \text{ kg h}^{-1}$  (filament speed  $20 \text{ cm min}^{-1}$ ) during the second laboratory extrusion. These production rates are dependent on factors such as solid content blended during extrusion, with screw speeds reaching up to 800 rpm while maintaining a controlled torque load below 80 %. The maximum temperature set for the screw mixing zones was 190 °C. Filaments with 4 different ceramic loadings i.e., 60 wt% (24 vol%), 70 wt% (33 vol%), 80 wt% (45.8 vol%) and 85 wt% (54.5 vol%) were extruded. From now onward, the filaments will be designated as F60, F70, F80, and F85, respectively (FXX = F: filament; XX: ceramic content in wt%). To ensure optimum printability, the filaments were dried at 60 °C and stored in a desiccator before use, to prevent/remove moisture absorption from the surrounding atmosphere. However, the filament F85 was not printable and hence could not be used for further study.

### 2.3. Rheological properties

The rheological properties of the pure binders and of the composite systems were studied at a temperature of 210 °C using the Rheograph 75 capillary rheometer (Göttfert, Germany) with a capillary length of 0.2 mm and a diameter of 0.5 mm for apparent shear rates ranging from 70 to 5800  $\text{s}^{-1}$ . The experimental procedure for the capillary rheometer utilized in our study consisted of the following steps:

- 1) filling the material into the capillary rheometer chamber;
- 2) heating it to the required temperature (210 °C);
- 3) allowing for a 4-minute temperature equilibration period, which was deemed sufficient for the heated volume;
- 4) automatic data collection of pressure readings once the material flow stabilized at pre-selected shear rates;
- 5) application of the Weissenberg-Rabinowitsch correction for the shear rates.

The shear rates and resolution of the flow curve were predetermined and set before measurements. In our approach, the measured shear range increased gradually on a linear scale and was examined through 9

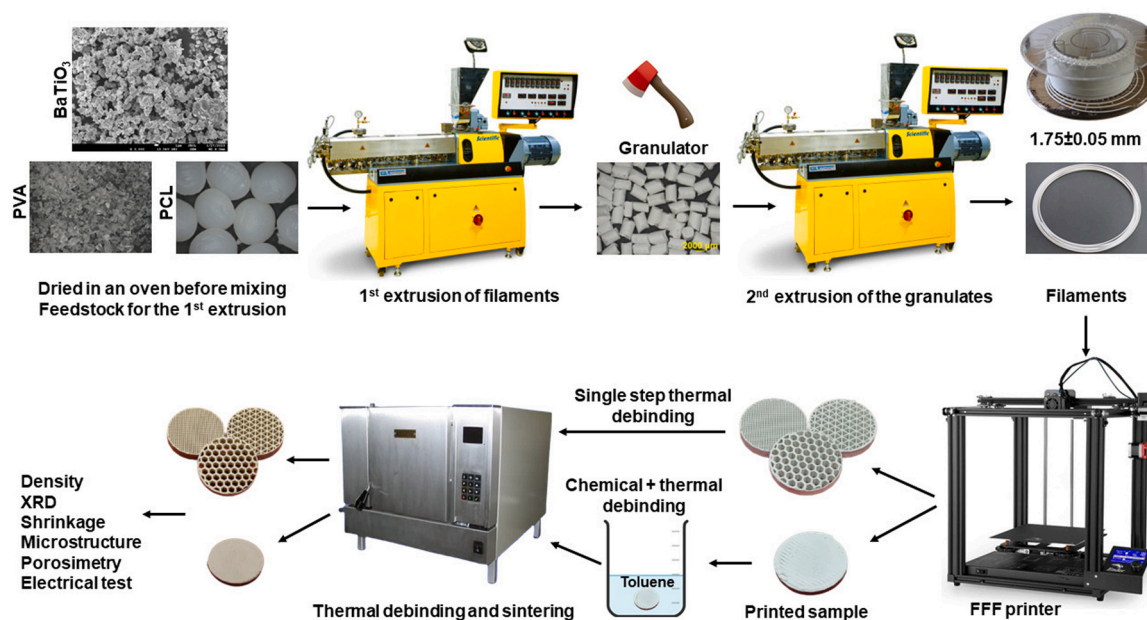


Fig. 1.. Overall schematic of the FFF of BaTiO<sub>3</sub>. Kindly note that the chemical debinding process is only meant for the dense 3D-printed discs. However, thermal debinding and sintering is mandatory.

measurements. The relative standard deviation error (RSD%) for this type of measurement typically stands at approximately 1.5 %.

The flow curves were fitted with Herschel - Bulkley model:

$$\tau = \tau_0 + k \cdot \dot{\gamma}^n \quad (1)$$

where  $\tau$  is the measured shear stress,  $\tau_0$  is the initial yield stress,  $k$  is the consistency factor,  $\dot{\gamma}$  is the true shear rate and  $n$  is the flow index. Weissenberg-Rabinowitsch correction is employed for a more accurate evaluation of the true shear rate; accordingly, the true shear rate is related to the apparent shear rate by:

$$\dot{\gamma} = \frac{3n + 1}{4n} \dot{\gamma}_a \quad (2)$$

#### 2.4. Characterization of the filaments

The filaments were broken by bending under cryogenic conditions and embedded in epoxy to observe the cross-section and the fracture surface of the filament. Images were collected with JSM-7500 F Cold FEG (JEOL, Japan) on polished and unpolished samples, after sputter coating with a thin layer of Au-Pd.

Ovality is determined by comparing the major and minor axes when examining the cross-section of the filament; for a perfectly round filament, the ratio between the two values is 1. More than 10 different sections of the extruded filaments were analyzed using an optical microscope, resulting in a range of min. and max. values.

Compressive mechanical testing of the filaments was carried out on mechanical tester SZ-3000 (Micro-Epsilon, Czech Republic). The 3 kN mechanical tester was equipped with custom-made collet-type holders allowing fast and reliable filament fixing. The tests were performed on filament segments with 40 mm length (while the distance between the gripping heads was set at 20.5 mm) at a constant strain rate of 2 mm min<sup>-1</sup>. At least 40 measurements were performed to statistically evaluate the mechanical properties of each filament. As the filament cross-section was not monitored for each measurement but rather assumed constant throughout all the measurements, the obtained results reflect nominal load and deformation dependencies. For each measurement, the maximum compressive stress (suggesting buckling) and the intrinsic Young's modulus (tangent at the load curve at very small compression, Fig. S4) were evaluated.

#### 2.5. FFF process

An Ender 5-Pro FFF printer (Shenzhen Creality 3D Technology Co, Ltd, China) with direct drive extruder (Micro Swiss, USA) equipped with a 0.4 mm and 0.3 mm brass nozzle was used for the fabrication of 15 mm (l) x 15 mm (w) x 5 mm (h) porous prisms with 25 vol% gyroid infill. In addition to these porous structures, dense discs with 15 mm diameter and height ranging from 1.8 to 3 mm were also printed to assess the potential for printing and debinding dense components; 1.8 mm high discs were also employed for dielectric and piezoelectric measurements. The 3D models were sliced with the help of PrusaSlicer-

2.5.0 software and the optimized parameters used for printing are listed in Table 1. No additional adhesives such as glue or tape were used to ensure good adhesion to the printing bed.

#### 2.6. Thermal analysis (TGA)

Thermogravimetric analysis (TGA) was carried out in STA 449 F5 Jupiter (Netzsch, Germany) using 10 – 15 mg of the extruded filament in an open Al<sub>2</sub>O<sub>3</sub> crucible in the temperature range of ambient temperature to 800 °C at a heating rate of 10 °C min<sup>-1</sup> in static air conditions to simulate similar conditions used for debinding in the furnace. This technique provides valuable information about the thermal decomposition of the binders used for fabrication of the filaments. Indeed, TGA data is very essential for designing the debinding cycles. In-depth analysis of the TGA curve (for e.g., DTG) helps in determining the specific temperature range where the maximum mass loss occurs. Overall, the TGA data plays a very crucial role in optimizing the debinding rate, temperature, and the holding time.

#### 2.7. Debinding and sintering

Samples printed under optimal conditions were first debinded (chemically or thermally) and then sintered at different temperatures to assess their relative density, morphological features, pore size, and functional properties. An additional chemical debinding process was implemented for the dense components, whereas only a single-step thermal debinding process was used for the porous components. In order to confirm the removal of the dissolvable component of the binder system during chemical debinding, Fourier-transform infrared spectroscopy (FTIR) was carried out on both extruded and chemically debinding filaments, using a Nicolet iS5 iD7 ATR FTIR Spectrometer (Thermo Fischer Scientific, USA) with a resolution of 4 cm<sup>-1</sup> and a spectral range of 4000 – 600 cm<sup>-1</sup>.

Based on the TGA analysis, the 3D printed samples were subjected to 5 different debinding cycles (discussed later, refer to Table S1) in order to determine the threshold (fastest) debinding rate for samples printed with the different filaments. In fact, the debinding rate affects samples with different solid content in a different way: filaments with a lower solid content will require slower debinding to avoid generation of cracks and defects. Optimization of debinding parameters allows to minimize the processing time and save energy. The debinding was carried out in a programmable laboratory furnace (Clasic CZ s.r.o., Czech Republic). A final temperature of 1000 °C was chosen to provide enough strength to the samples during handling.

After the debinding process, the samples were subjected to the desired sintering temperatures (1200 °C, 1250 °C, 1300 °C, 1350 °C) using high-temperature furnace SF-1 (Swedish Furnace AB, Sweden) at a heating rate of 10 °C min<sup>-1</sup> with a holding time of 2 hours. Once the sintering process was completed, the furnace was cooled to room temperature by spontaneous cooling before taking out the samples. To prevent undesired reactions between the substrate and the sample, the latter were placed on 3YSZ scaffold structures during high-temperature sintering.

To compare the selected physical properties of the printed components with those produced conventionally, the BaTiO<sub>3</sub> powder was mixed with PEG (2 wt%) and then uniaxially pressed at 5 MPa using a 10 mm diameter die. Subsequently, the pressed discs were debinded at 550 °C with a ramp of 1 °C min<sup>-1</sup> and sintered under similar conditions as the 3D printed samples.

#### 2.8. Samples characterization

Optical microscopy was performed using an optical microscope Stemi 508 coupled with an Axiocam 105 camera (Carl Zeiss, Germany) with magnifications from 0.63 to 5x at all stages of the process. The thickness of strut deposited with different nozzles was measured from

**Table 1**  
Printing parameters used during FFF of the composite filaments.

Parameters	Value
Printing speed	10 mm s <sup>-1</sup>
Nozzle temperature	210 – 230 °C
Bed temperature	Room temperature
Vertical shell perimeter	1
Infill geometry	Porous: Gyroid Dense: rectilinear
Infill density	Porous: 25 % Dense: 100 %
Nozzle diameter	Porous: 0.3 mm, 0.4 mm Dense: 0.4 mm
Skirt	Yes, 3

the collected images and is reported as an average of at least 20 different measurements. The density of the sintered specimens was measured using the Archimedes principle using water as a buoyant medium. Additionally, the shrinkage of the sintered components was measured with digital calipers. The shrinkage measurements have been recorded for 3 samples each for different filament and sintering temperature.

Phase analysis of the samples fabricated with F70 was carried out in  $\theta$ -2 $\theta$  diffractometer D8 Advance (Bruker, Germany) in the  $2\theta$ -range of  $20 - 70^\circ$  ( $\Delta(2\theta) = 0.02^\circ$  with a scan time of 1 sec/step) using Cu  $K_\alpha$  radiation ( $\lambda=1.5418 \text{ \AA}$ ). The X-ray source operated at 40 kV and 40 mA. Raman spectra was recorded with a ThermoFisher DXR3xi Raman Imaging Microscope, using a 532 nm laser with a  $10 \times$  objective.

A mercury intrusion porosimeter Poremaster 60GT (Quantachrome, UK) was used to determine the pore size and distribution of the sintered samples. Fragments of sintered components, usually smaller than 10 mm in diameter, were used for the tests. The maximum applied pressure of mercury was 414 MPa, which is equivalent to the Washburn pore radius of 1.8 nm. For comparison, a powder-pressed disc sintered at  $1300^\circ\text{C}$  was used.

The sintered samples were grinded and polished with diamond paste down to  $3 \mu\text{m}$  and thermally etched in air at a temperature of  $1195^\circ\text{C}$  for 1 hour. The microstructural analysis of the polished samples coated with sputtering (thin layer of Au-Pd) was carried out in JSM-7500 F Cold FEG (JEOL, Japan) and analyzed via the freeware image processing software ImageJ [44].

The dielectric properties of the 3D printed and sintered ceramic discs were measured with the broadband dielectric spectrometer Concept 40 (Novocontrol Technologies GmbH, Germany) in the frequency range of 0.1 Hz to 1 MHz at room temperature. The samples (after debinding and sintering) for the dielectric spectroscopy were disk-shaped with a diameter of around 10 – 12 mm and ground to a thickness of  $\sim 1 \text{ mm}$ . As a test cell, the BDS-1200 parallel-plate capacitor with two gold-plate electrodes was used. Additionally, the discs were gold plated on the two opposing surfaces before using it in the test cell.

The electromechanical properties of the samples were characterized using a TF Analyzer 2000 (aixACCT Systems GmbH, Germany). Before measuring the samples under an electric field, the disk-shaped samples were sputtered with gold on their parallel faces. The precise area of the electrodes was determined using a digital light microscope (Keyence). The small signal analysis was performed on the unpoled samples to obtain the piezoelectric coefficient ( $d_{33}$ ), while the large signal analysis was used to obtain the ferroelectric polarization (P) and the electromechanical strain (S). All measurements were taken at 2 kV/mm bipolar electric field with a frequency of 1 Hz for large signal measurements and 1 kHz for small signal measurements. Large signal measurements for the determination of the electromechanical response of the material are performed by applying a high electric field in the order of kV/mm and measuring the electric field induced strain and polarization (large signal). Small signal measurements for the determination of the dielectric properties are performed by applying a bias field in the order of kV/mm and superimposing an oscillation with an amplitude of the order of V/mm to measure the piezoelectric coefficient.

### 3. Results and discussions

#### 3.1. Characterization of the composite filament

##### 3.1.1. Diameter, ovality, cross-section and fracture, surface smoothness

Tight tolerances in filament diameter and cross-section are crucial for ensuring consistent and accurate volumetric flow rates during printing. When the diameter is smaller or larger than the specified value in the slicing software, under- or over-extrusion occurs, respectively. Such inaccuracies lead to defects or decreased resolution in the printed parts. The nominal diameter of the extruded filaments through the extruder nozzle, measured with a digital caliper, was  $1.75 \pm 0.05 \text{ mm}$ , which is in perfect agreement with the commercially available polymer-

based ones.

The assessment of filament ovality is another crucial step in ensuring the quality and uniformity of the filament production required for top reproducibility of 3D printouts. The dimensional exactness of the filament cross-section can be verified, and process adjustments can be made if it is not circular. The filament production process in a laboratory typically involves the use of a winding device; its speed dictates the final diameter of the filament and can be manually adjusted. However, significant discrepancies between the desired final diameter and that of the material exiting the extruder die could result in an ellipsoidal cross-section shape. The obtained filaments were cryogenically fractured in nitrogen and then embedded in the resin (Fig. 2(a-c)), to check for ovality and possible defects, such as pores trapped during the production process [30]. Ovality values for all filaments are in the range of 0.993–0.995, which is extremely close to the target value for a perfectly round filament (ovality = 1).

In a high-quality filament, the ceramic particles should be evenly distributed in the polymer matrix without heterogeneities such as agglomerates. In addition, good adhesion between the matrix and the particles ensures that the latter remain embedded in the filament when it is exposed to high shear stresses during printing; otherwise, phase-separation can occur [33,34]. The double extrusion process employed in this study ensures the homogeneous distribution of the ceramic phase, as can be observed from the fracture surfaces of the filaments (Fig. 2(d-f)). The homogeneous distribution of particles, together with a right choice of extrusion temperature, ensures that the filament surface is smooth, as seen in Fig. 2(j-l); the limited roughness guarantees a high surface finish and overall quality of the printed objects. Only the F80 filament (Fig. 2(i)) exhibits noticeable agglomerates (marked with yellow circles), possibly due to an insufficient amount of polymer matrix to bind the ceramic particles. The agglomerates resulting from the insufficient amount of the thermoplastic binders for the ceramic powders are only visible at microstructural level and do not protrude out of the filaments. Hence, it does not significantly affect the roughness of the filament to a great extent as visible in Fig. 2(i). The eventual presence of agglomerates will influence the rheological and mechanical properties, as will be discussed in the following paragraphs.

##### 3.1.2. Rheological behavior of the composite

The rheological properties of the filaments guide the flow behavior during the extrusion process. Fig. 3 shows the (a) apparent shear viscosity and (b) the shear stress as a function of shear rate, measured at  $210^\circ\text{C}$  to simulate the printing conditions. The polymeric binders that constitute the matrix exhibit intrinsic shear thinning behavior (decreasing viscosity/decreasing the slope of the shear stress curve with increasing shear rate), consistent with their thermoplastic nature. At low shear rates, polymeric chains are arranged in a somewhat random or entangled configuration, resulting in high viscosity. As the shear rate increases, the polymeric chains experience a higher level of deformation or strain. This leads to disentanglement and alignment of the polymeric chains in the direction of the flow, resulting in a reduction of the viscosity. For very high shear rates, the viscosity can approach a plateau as complete alignment is reached; this is the case with binder B. The addition of ceramic powder to the binder system had a notable effect on the rheology. With increasing ceramic loading from F60 to F80, the viscosity increased gradually and the shear thinning behavior became more pronounced (the flow index  $n$  decreases from  $0.61 \pm 0.05$ – $0.34 \pm 0.04$  with increase in the ceramic loading). A remarkable surge in viscosity (one order of magnitude compared to the pure binder) was observed in the filament F80. With a higher ceramic loading, the ceramic particles are more densely packed, resulting in increased interparticle interactions between them. This increased contact leads to a larger resistance to flow, thus causing an abrupt increase in viscosity. Moreover, such proximity can result in the onset of shear thickening behavior at high shear rates, as expressed by the slight bump in viscosity at  $1000$ – $2000 \text{ s}^{-1}$ . Khatri et al. reported that it was not possible to print

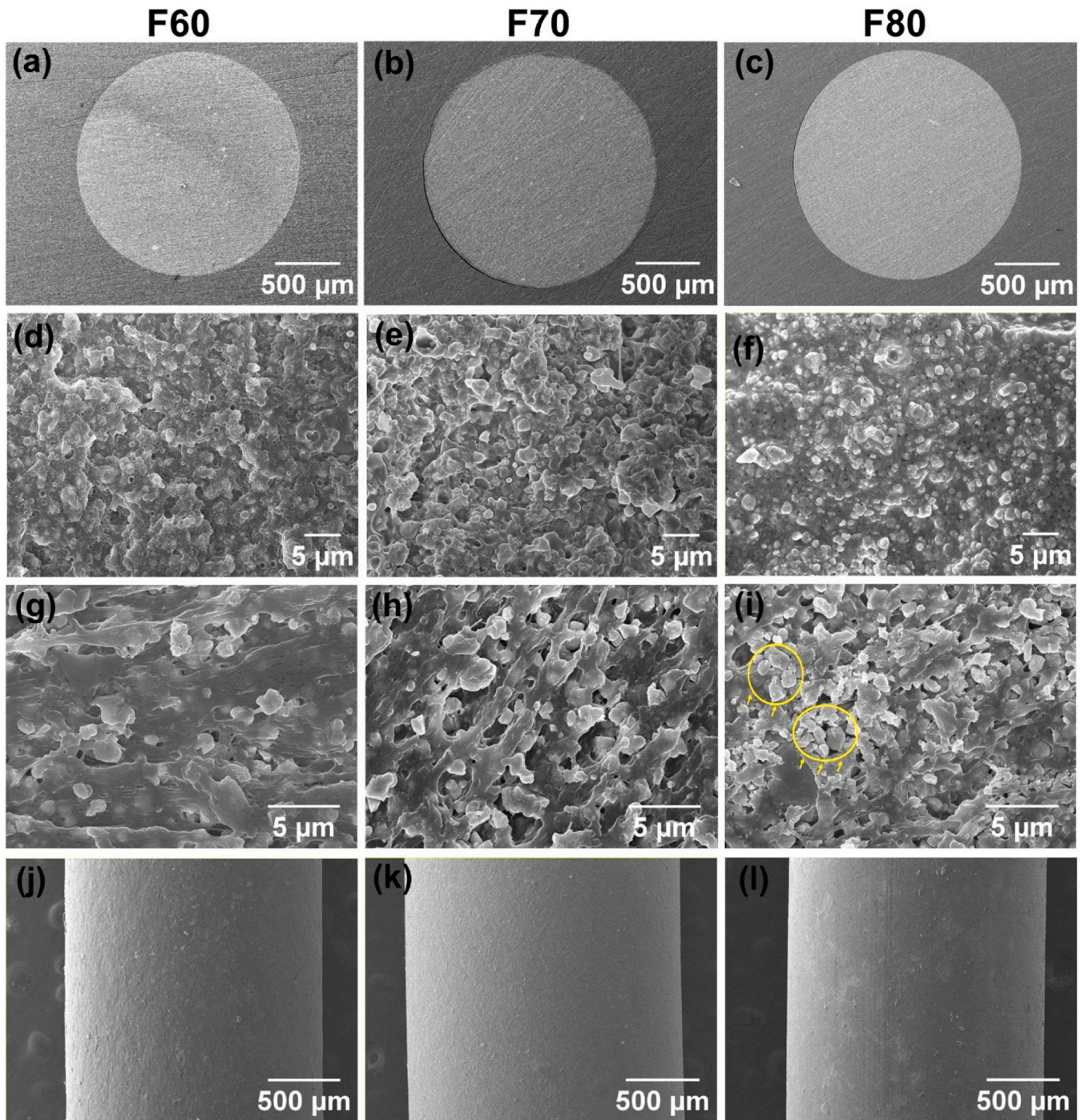


**Fig. 2.** (a-c) Overview SEM images of the cryogenically fractured and grinded cross-section of the filaments. (d-f) Magnified SEM images of the cryogenically fractured filaments showing no defects. (g-i) Magnified SEM images of the cross-section exhibiting the distribution of particles in the thermoplastic matrix. (j-l) Overview SEM images of the external surface of the extruded filaments.

filaments with more than 35 vol% of BaTiO<sub>3</sub>; increasing the ceramic content led to a very brittle filament with frequent breakage at the gripping motors and exhibited stick-slip phenomenon [31]. Lower ceramic loadings limit the probability of the particles touching each other, as could be observed from the microstructures in Fig. 2(d-i).

The measured rheological properties of the filaments suggest that they are good candidates for FFF: in fact, they exhibit shear thinning behavior with viscosities compatible with extrusion through a fine nozzle at the temperature and shear rates that are typically achieved while printing (210 °C, 100 – 2000 s<sup>-1</sup>) [45]. Based on the printing conditions and the printer nozzle diameter, the apparent shear rates ( $\dot{\gamma}_a$ )

can be estimated with the following equation:

$$\dot{\gamma}_a = \frac{4Q}{\pi R^3} \quad (3)$$

where  $Q$  is the volumetric flow rate (mm<sup>3</sup> s<sup>-1</sup>) and  $R$  is radius of the nozzle (mm). The volumetric flow rate can be calculated using the width of the extrusion (mm), layer height (mm) and the print speed (mm s<sup>-1</sup>). This gives rise to an apparent shear rate in the range of 128 – 144 s<sup>-1</sup> for a nozzle of 0.4 mm diameter and 227 – 264 s<sup>-1</sup> for a nozzle of 0.3 mm diameter. The true shear rate values slightly increase to 139 – 210 s<sup>-1</sup>

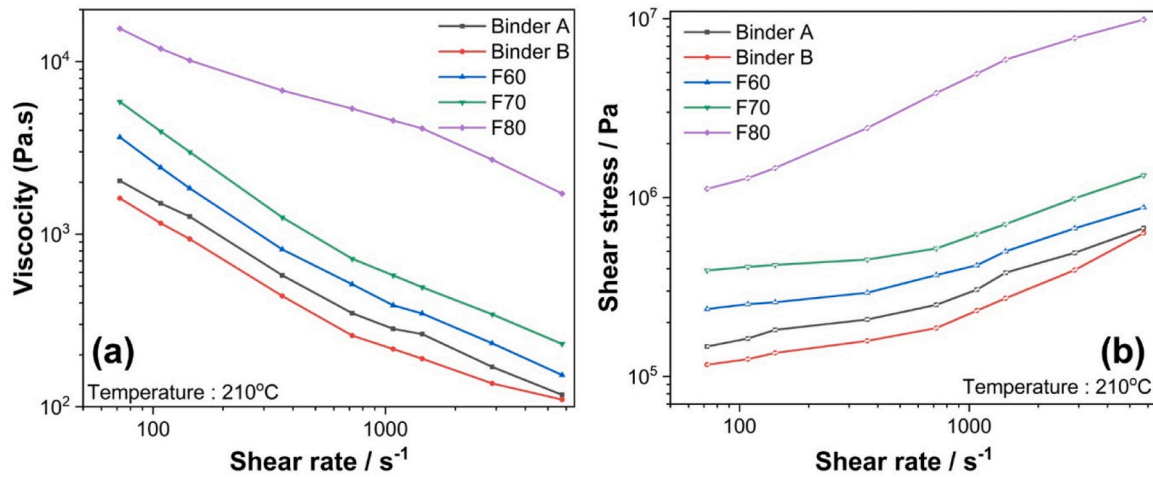


**Fig. 3.** Flow curves of the pure binders and the composite system: (a) Viscosity and (b) Shear stress as a function of shear rate of the pure binders and composite system with various levels of solid loading. Curves were measured at a temperature of 210 °C to simulate similar thermal conditions during printing.

for 0.4 mm nozzle diameter and 247 – 301 s<sup>-1</sup> for 0.3 mm nozzle diameter. It is important to note that this calculation does not consider filament retraction during the printing, where the filament rates may reach around 100 mm/s, corresponding to shear rates of approximately 2000 s<sup>-1</sup>.

### 3.1.3. Compressive mechanical testing

During FFF printing, the most common failure mode consists of filament buckling, which usually occurs between the feeding rollers and the printing head, connected to the construction details of the respective printer [46]. Extrusion through the nozzle requires a certain pressure drop ( $\Delta P$ ), which varies with the viscosity of the feedstock, the geometry and size of the nozzle orifice, and the flow rate. If this pressure drop is larger than a critical value, buckling will occur and interrupt the printing process. The critical pressure required for buckling,  $P_{cr}$  is described by the Euler buckling analysis equation [47]:

$$P_{cr} = \frac{\pi^2 E d_f^2}{16 L_f^2} = \frac{\pi^2 E}{16 \left(\frac{L_f}{d_f}\right)^2} \quad (4)$$

Where  $E$  is the elastic modulus of the filament,  $d_f$  is its diameter and  $L_f$  is the length between the feeder rollers and the entrance of the printing head.  $P_{cr}$  is strongly dependent on the elastic modulus of the filament (under compression) and the slenderness ratio ( $L_f/d_f$ ). For filament with constant elastic modulus, the increase in slenderness ratio  $L_f/d_f \gg 1$ , the critical pressure  $P_{cr}$ , for buckling to occur reduces [40]. The slenderness ratio should be as small as possible such as in Direct drive printers in comparison to Bowden printers; however, this is a construction feature of the 3D printer equipment and must be considered before the printer purchase. To minimize the risk of failure, it is helpful to have filaments with a high elastic modulus  $E$ .

To simulate the conditions experienced in the FFF printer, compressive tests were performed on the different filaments with a mounting distance of  $20.5 \pm 0.05$  mm between the gripping heads. Typical load-displacement curves are reported in Fig. 4; the Young's

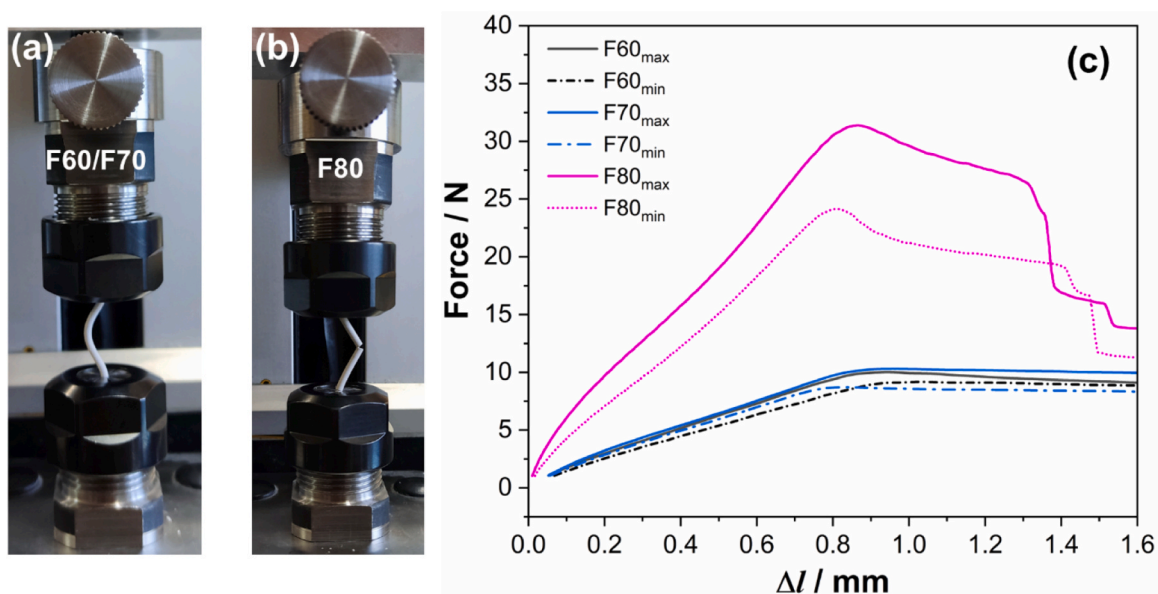


**Fig. 4.** Compression test set up for the fabricated filaments showing the buckling/fracture behavior for filaments (a) F60 and F70 (b) F80. (c) Typical force vs displacement curves for the filaments. Please note that for each of the filaments, the curves with maximum and minimum slopes have been represented.

modulus and the critical stress before buckling were extrapolated and are reported in Table 2. More details about the statistical analysis of the measurements can be found in the supplementary (Fig. S4). Initially, at lower compressive displacement, the relationship between load and displacement is linear, suggesting that the deformation is elastic. As the displacement increases further, the filaments (F60 and F70) buckle and then deform plastically (horizontal plateau), but they do not break in the range tested (up to 1.6 mm). Conversely, the filaments with higher ceramic loading (F80) exhibit a drop in applied load after the linear trait, indicating a fracture. The reason for the different behavior is rooted in the microstructures of the filaments (Fig. 2). In filaments with lower ceramic contents (F60, F70), ceramic particles are homogeneously dispersed and do not come into contact with each other, thereby preventing the formation of a percolating phase; the polymer matrix phase remains continuous. Conversely, in filaments with higher ceramic loading (F80), the particles make contact, creating a percolating phase; the filaments then exhibit a higher tendency to break instead of buckle when the stress exceeds the critical value. With even higher ceramic loading (F85), the filament broke already when entering the feeder rollers. Therefore, a compromise between high ceramic loading and brittleness is essential to ensure a smooth printing process without failures. Filament critical stress serves as a valuable indicator of filament printability, particularly when utilized in FFF printers equipped with direct drive filament feeding systems. When combined with other physical parameters, such as viscosity, these values offer insight into the filament's performance. In addition, critical values for Young's modulus and compressive stress are typically unavailable for experimental published data or commercial filaments datasheets. Therefore, it is essential to report these values as significant technical performance indicators. Here, the composite system with an upper filler loading of 80 % exhibited a critical stress of approximately 9 MPa and a Young's modulus of around 500 MPa; for a filler loading of 60 % the critical stress decreased to approximately 3 MPa and the Young's modulus to about 100 MPa. The reported values in Table 2 for F60 and F70 are notably lower than the laboratory prepared HAP and commercial PLA-g filaments reported in [40]. F80 values correspond to those of the HAP-1 filaments, yet they remain consistently lower than those of the commercial reference. Despite the differences, all BaTiO<sub>3</sub> filaments fell within a printable range, with a maximum viscosity upon extrusion of 9–10 kPa•s for F80 and a minimum one of 1–2 kPa•s for F60.

While mechanical tests on 3D printed objects are commonly reported in publications [31], focusing on mechanical anisotropy due to the layer-by-layer forming principle, a standardized procedure for filament mechanical tests across producers including experimental filament studies remains elusive. It's important to note that our objective was not to verify filament welds but rather to highlight conditions under which filament buckling in direct drive printers could lead to 3D printing failures and to gather the necessary experimental data to address this issue.

### 3.1.4. Thermal analysis of the filaments

Fig. 5 reports the thermal decomposition behavior of the extruded composite filaments. The weight loss of the filaments at low temperatures is attributed to the removal of volatiles and moisture, also evidenced from the presence of a very broad FTIR peak at 3310 cm<sup>-1</sup>, corresponding to stretching vibration of water (see Fig. 8(b)). Associated with the hygroscopic nature of PVA, moisture can lead to significant

**Table 2**  
Critical stress before buckling and Young's modulus of the different composite filaments.

Filament	P <sub>cr</sub> [MPa]	E [MPa]
F60	3.5 ± 0.5	102 ± 18
F70	4.4 ± 0.6	169 ± 28
F80	9.6 ± 1.8	556 ± 72

problems while printing, such as formation of bubbles and bulges on the extruded filament (Fig. S6) [48]; hence, the filaments were dried in a dryer at 60 °C for up to 12 hours and stored in a desiccator before printing.

With increasing temperature, the polymers in the binder start to decompose with a convoluted process resulting from the overlapping of multiple decomposition steps characterizing both polymers in the blend (Fig S5). The first DTG peaks detected fat ~ 300 – 320 °C and 350 – 400 °C could include decomposition of residual acetate groups followed by backbone breakdown in PVA, and ring opening and ester pyrolysis reactions in PCL; 40 – 50 % of the total mass loss already occurs in correspondence to the first peak. The peak(s) at ~ 400 – 480 °C correspond to the oxidation and release of carbonaceous species, i.e. the completion of pyrolysis processes; no significant mass loss is observed after this point.

With increasing ceramic loading, the peaks in the DTG shift toward lower temperatures; this is particularly evident for the peaks at higher temperatures: the mass loss completion occurs for F80 at ~400 °C, i.e., ~100 °C lower than for F60. The lower decomposition temperature is associated with a catalytic decomposition effect at the solid surface of used BaTiO<sub>3</sub>, observed also for other types of oxides such as Al<sub>2</sub>O<sub>3</sub>, TiO<sub>2</sub>, Cr<sub>2</sub>O<sub>3</sub>, SiO<sub>2</sub> etc. [49,50]. This effect is more prominent in air as opposed to inert atmospheres. In addition, such phenomenon has also been verified in a recent study using mullite (3Al<sub>2</sub>O<sub>3</sub>.2SiO<sub>2</sub>) filaments [38].

Fig. 5(d) compares the residual mass observed from TGA analysis to the theoretical one; corresponding volumetric contents are also reported. As the solid loading increases, a discrepancy between theoretical and measured values starts to occur; this manifests technology limitations resulting in inhomogeneous mixing derived from the high torque generated in the extruder and low amount of polymeric binder present that could not wet the surfaces of the ceramic particles. In fact, the higher ceramic loadings (F80, F85) resulted in an increase in the torque exerted by the screws during the composite mixing process, which exceeded 80 % of the maximum torque accepted by the equipment. Higher torque may lead to extruder failure and inhomogeneous mixing; therefore, it was not possible to introduce a higher ceramic content than in F85.

### 3.2. Printability assessment

Printability is a broad concept, which encompasses user-friendly manipulation, filament flexibility, ease of extrusion, and the achievement of high-quality printed surfaces and designs. A convenient and rapid method to assess the printability of filaments is by examining the surface of the filament after it went through the feeder gears: when the gears drive the filament into the nozzle, they clutch at its surface, damaging it. Fig. 6 shows an overview of SEM images of both a printable (F70) and a non-printable filament (F85), highlighting the differences in their surface features. In the first case (Fig. 6(a-b)), distinct gear tooth marks can be seen; they are regular and shallow and do not affect the filament behavior. The non-printable filament, on the other hand, shows extensive surface grinding, with irregular and rough gear tooth marks (Fig. 6(c-d)); the excessive removal of material from the surface does not guarantee good gripping of the feeder gears, generating inconsistencies in the printing process.

Triply-periodic minimal surface such as the gyroid pattern was printed using the printer parameters listed in Table 1 (Fig. 7). The extrusion temperature is set in a range of 210 – 230 °C (well below the onset of binder decomposition, Fig. 5(a-c)). The nozzle size plays a crucial role in determining the resolution and overall quality of the printed objects; moreover, it influences the printability of the filament. In fact, the pressure drop in the nozzle strongly increases with decreasing nozzle size, according to the Hagen-Poiseuille law [51]. Moreover, the ceramic powder size should also be significantly smaller than the nozzle to avoid clogging.

First, a brass nozzle with a diameter of 0.4 mm was used as the

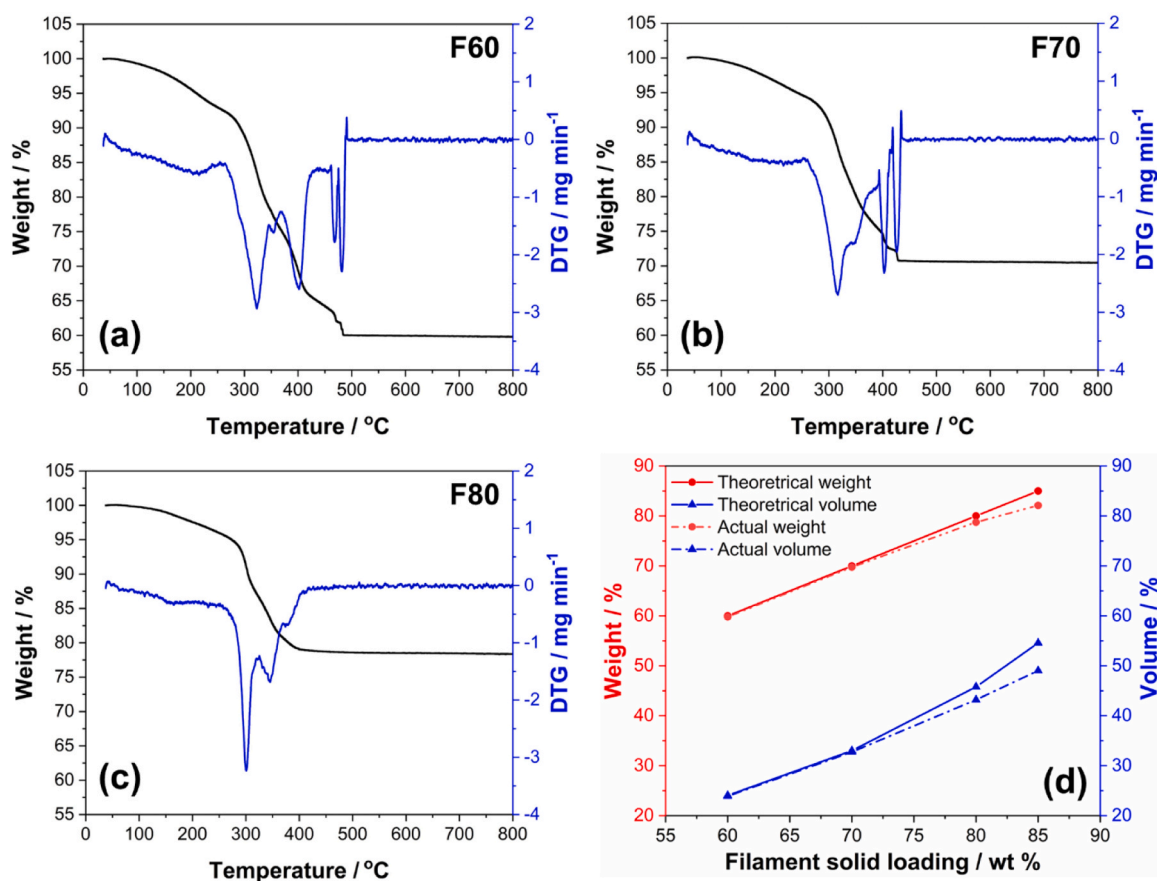


Fig. 5. Thermo-gravimetric analysis (TGA) of the fabricated filaments with (a) 60 wt% (b) 70 wt% (c) 80 wt% of BaTiO<sub>3</sub> powder. The analysis was carried out in air with a heating rate of 10 °C min<sup>-1</sup>. (d) Correlating the residual ceramic content in terms of weight and volume percent to the theoretical value.

standard diameter for FFF. With the exception of F85, no evidence of nozzle clogging and filament breakage was observed (see resulting samples in Fig. 7(a)). The printing temperature was set at 210 °C for all filaments; in the calculated shear rate range, they possessed a viscosity of 1.4–12 kPa s. A smaller (0.3 mm) nozzle was then object of testing; the gyroid pattern was adapted to account for the smaller feature size and maintain the same nominal porosity in the samples. In fact, as seen in Fig. 7(b), the smaller nozzle size enables the deposition of thinner lines and layers, which can be particularly advantageous when printing intricate designs or small-scale objects. The thickness of the deposited struts was measured to be  $0.44 \pm 0.03$  mm and  $0.34 \pm 0.02$  mm for the 0.4- and 0.3-mm nozzle, respectively. However, only the filaments with lower ceramic loadings (F60, F70) could be printed, with a slight increase in the extrusion temperature up to 225 °C for F60 and 230 °C for F70 to ensure a smooth flow. Nozzle clogging and flow interruption frequently occurred while printing with filament F80.

### 3.3. Debinding of printed samples

The binder removal process is usually the most delicate, time-consuming, and energy-intensive process. In fact, slow heating ramps are required to ensure that the expulsion of the binder does not generate defects in the samples. The surface-to-volume ratio in the printed part plays a key role: porous structures, such as the gyroids proposed here, provide a well exposed surface from which the binder can be easily released. However, when it comes to denser discs or structures, binder removal becomes more challenging. If the amount of binder present in the samples is excessive, even slow heating ramps may result in bulging of the samples. Bulging occurs as a result of the expansion of gases (generated by binder decomposition) that remain entrapped in the

sample. A possible solution is the partial removal of the binder through a chemical process prior to thermal debinding. Here, bulk samples were soaked in toluene at room temperature for up to 3 h and allowed to dry before undergoing thermal debinding and sintering.

None of the dense components printed with F60 filament could survive the thermal treatments even after undergoing the chemical debinding step as evidenced in Fig. S3; therefore, they were not characterized further. The weight loss associated with chemical debinding of F70 and F80 filaments for different times was evidenced by the TGA measurements (Fig. 8(a)): as expected, F80 filaments showed a lower mass loss (~2.65 wt%) than F70 (~3.45 wt%) due to the overall lower amount of binder. While the binder removal was only partial, it did not seem to progress significantly from 1 h to 3 h soaking time; nevertheless, a 1 h chemical debinding allowed both F70 and F80 samples to survive the subsequent thermal treatments. FTIR measurements (Fig. 8(b)) performed on F70 confirmed binder removal: the decrease in intensity of the FTIR signal observed in chemically debinded samples indicates a reduction in the presence of certain chemical bonds or functional groups (2917 and 2847 cm<sup>-1</sup> for C-H stretching, 1720 cm<sup>-1</sup> for C=O stretching, 1000–1250 cm<sup>-1</sup> C-O stretching).

The TGA/DTG analyses performed on filaments for assessing their printability (see Fig. 5) also guide the design of an efficient thermal debinding process. The peaks associated with moisture release, binder decomposition and oxidation of carbonaceous species appear below 200 °C, at ~ 300–320 °C and ~ 400–480 °C, respectively; a slow heating rate and a dwelling step at such temperatures should ensure gradual removal of organics and maintain the integrity of the printed structure. The debinding rates have been carefully chosen so that the process is slower in the temperature range 180–300 °C; in fact, 40–50 % of weight loss occurs within this temperature range. It is postulated that

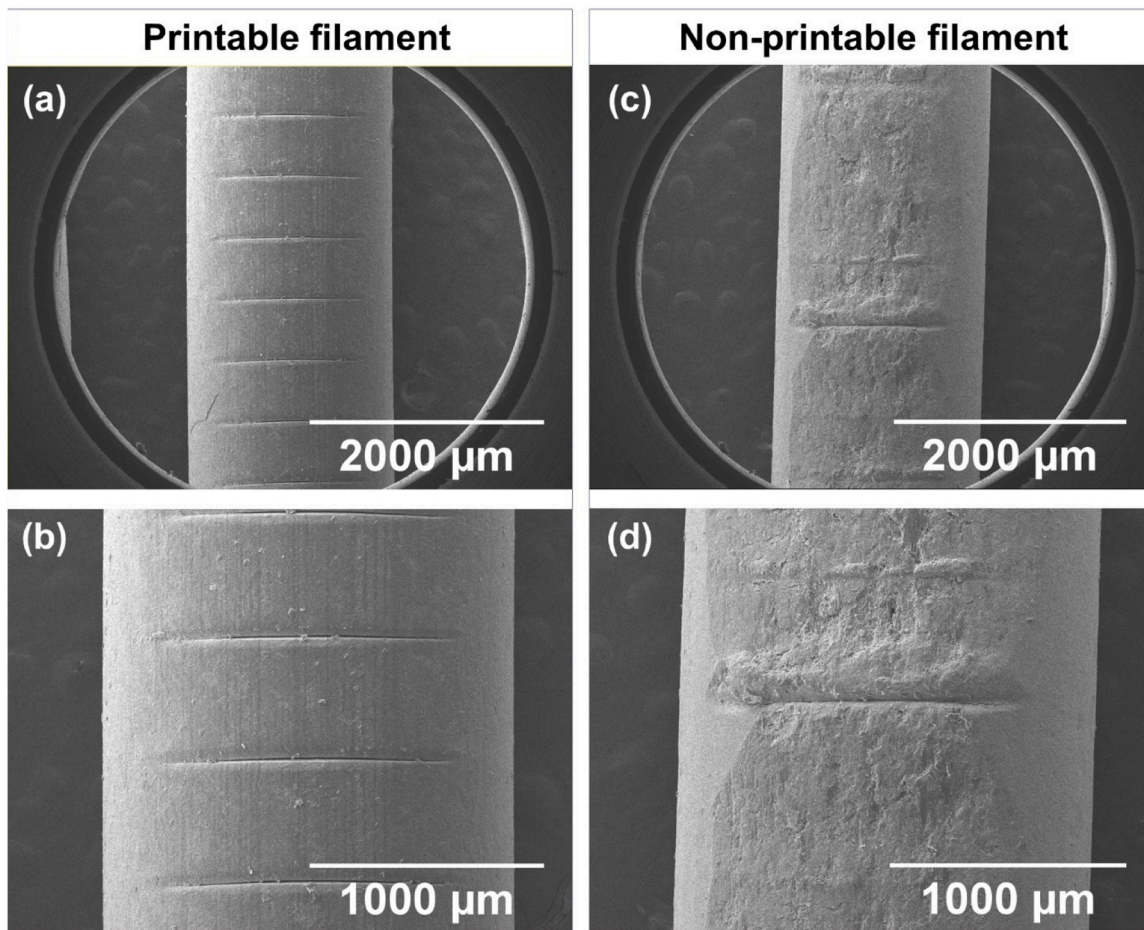


Fig. 6.. Overview SEM images showing a clear difference between (a, b) a printable and (c, d) non- printable filament. The printable filaments have regular and shallow gear tooth marks; on the other hand, the non-printable filaments exhibit a ground surface with irregular and rough gear tooth marks.

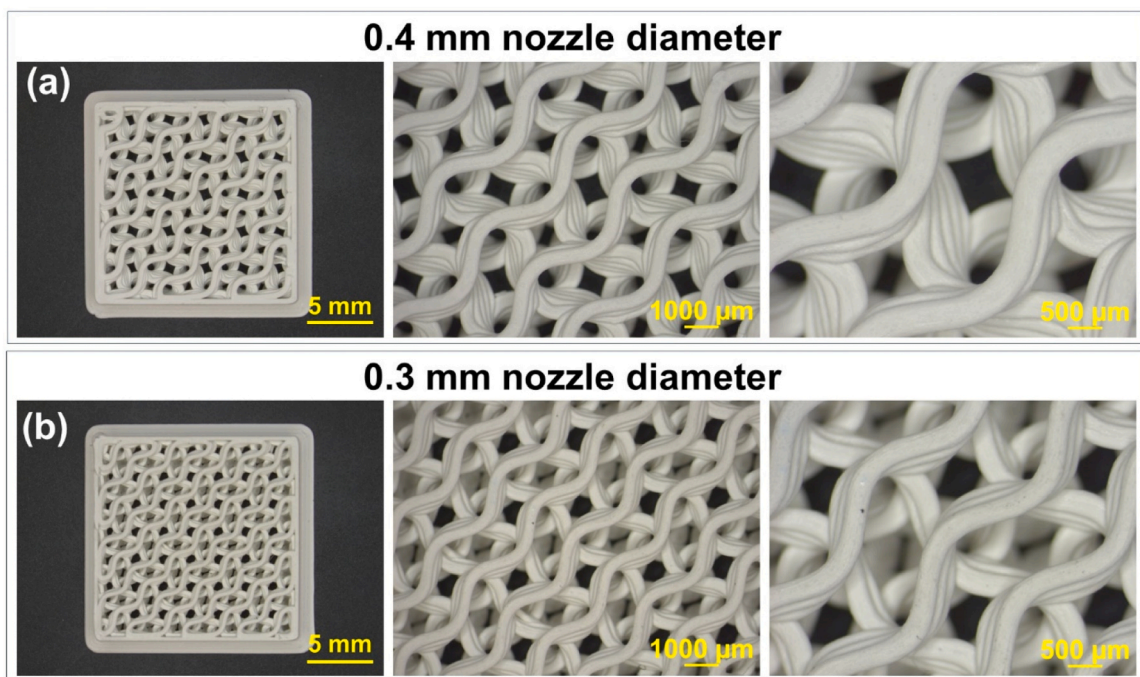
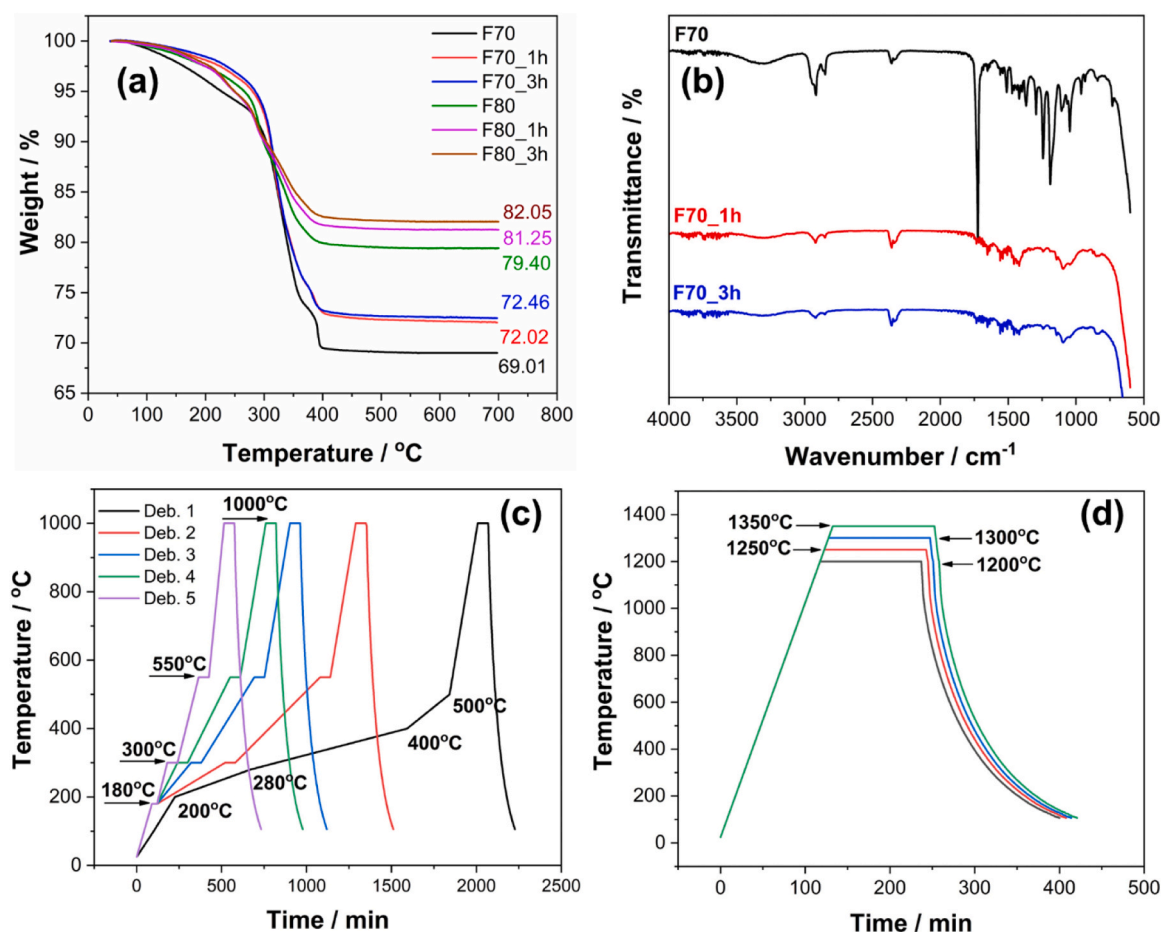


Fig. 7.. Optical images of the samples printed using (a) 0.4 mm and (b) 0.3 mm nozzle diameter. The layer thickness was set to 0.2 mm. Highly magnified image clearly shows the difference in the width of extruded struts.



**Fig. 8.** (a) Thermo-gravimetric analysis (TGA) of F70 and F80 filaments, as-fabricated and after chemical debinding in toluene for 1 h and 3 h at room temperature. (b) Fourier Transform Infrared Spectroscopy (FTIR) analysis of F70 filament, as-fabricated and after chemical debinding in toluene for 1 h and 3 h at room temperature. (c) Different thermal debinding regimes used in this study to debind the printed samples. (d) Different sintering profiles used for the debinded samples. Please note that the samples were cooled down to room temperature naturally.

the onset of defects occurs mainly in correspondence to the first DTG peak ( $\sim 300 - 320^\circ\text{C}$ ). For this reason, with the aim to identify the threshold heating rates for filaments with different ceramic loadings, different ramps were tested in the range  $0.1 - 2^\circ\text{C min}^{-1}$ . The open porosity resulting from the partial binder burn out in this first region facilitates the subsequent removal of the remaining binder at higher temperatures by providing a pathway for gas release [52]; hence, a significantly higher heating rate was implemented in the temperature range  $300 - 550^\circ\text{C}$  from Deb. 2 onwards.

Fig. 8(c) reports the various debinding cycles used in this study. While the initial and the final debinding steps are consistent for all debinding cycles (except for debinding regime 1), the heating rates in the temperature ranges  $180 - 300^\circ\text{C}$  and  $300 - 550^\circ\text{C}$  vary (Refer to table S1).

Debinding cycle 1 was used in the initial stages of the project, prior to TGA / DTG analysis. From debinding regimes 2–5, the goal was to decrease the total time required for the cycle while still reliably obtaining dense and defect-free structures. While TGA results showed that the binder decomposition is nearly completed in the range of  $400 - 500^\circ\text{C}$  (depending on the ceramic loading), a higher final debinding temperature of  $1000^\circ\text{C}$  was chosen to ensure complete removal of the binder from the printed object, considering its size and geometry. Moreover, the onset of sintering should impart sufficient strength of the produced green bodies and ensure that they could be handled and moved from the debinding to the high-temperature furnace.

A qualitative assessment of the effect of the various debinding cycles is reported in Fig. 9 and Table 3. The survivability of the sample during

the binder burn out process using different debinding cycle has been determined by the presence of defects in forms of blistering or delamination after carefully observing through an optical microscope. The presence of a single defect alone was considered enough to discard the sample. All the samples, regardless of their porosity and filament composition, survived the debinding regimes 1 and 2 without noticeable defects.

The dense 3D-printed discs could only survive when printed with F70 and F80 filaments and subject to debinding regimes 1 and 2. Discs with different heights (from 1.8 to 3 mm) were printed in order to determine the maximum thickness that could be successfully debinded. With the slower treatment (debinding regime 1), F80 yielded defect-free samples with a maximum thickness of 2.2 mm; for F70, samples with a thickness of 2 mm survived but presented minor blistering. The remaining samples were either blistered or delaminated. Upon increasing the heating rates (as with debinding regime 2), the maximum thickness decreased to 2 mm for F80 and 1.8 mm for F70 samples.

The remaining cycles were tested only on the porous structures. Upon debinding with debinding regime 3, F60 samples started exhibiting blistering or bulging resulting from fast gas release (marked). Further increasing the heating rates (debinding regimes 4 and 5), blistering in F60 samples became more severe and was accompanied by structure deformation. The onset of defects shifted to higher heating rates for F70 samples and remained moderate also for the fastest debinding regime (5). The F80 samples were not affected by all the debinding regimes tested.

To guarantee consistent debinding conditions for all samples,

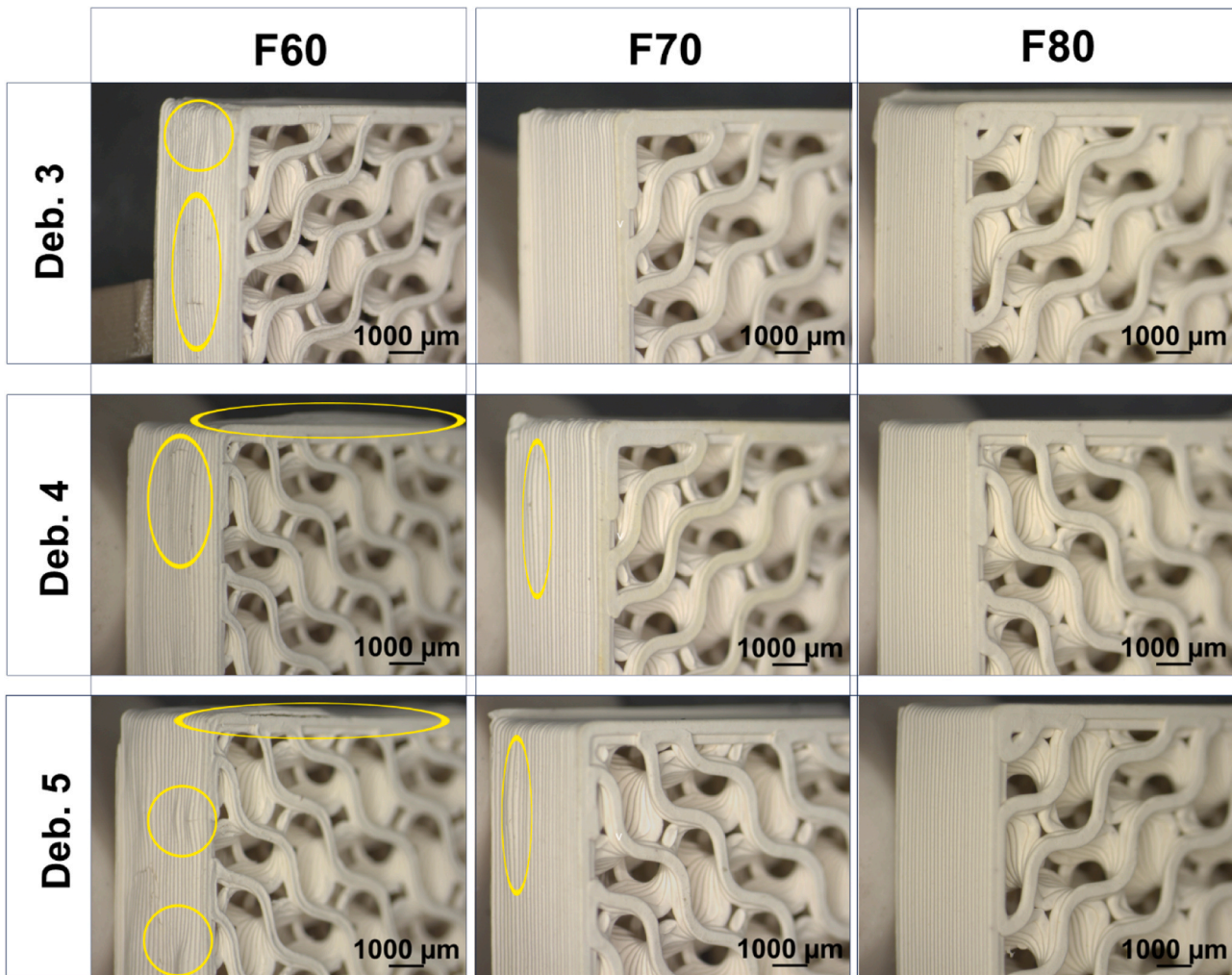


Fig. 9.. Optical images of the samples subjected to different debinding regimes. Kindly note that these samples were only thermally debinded.

**Table 3**

Summary of the thermal debinding results for the porous samples. The corresponding optical images are depicted in Fig. 9.

Debinding regime	Result		
	F60	F70	F80
Deb. 1: Ultra-slow	No visible defects,	No visible defects,	No visible defects,
Deb. 2: Slow	Structure retained	Structure retained	Structure retained
Deb. 3: Moderate	Blistering, Deformation		
Deb. 4: Fast	Severe blistering, Severe deformation	Minor blistering, No deformation	No blistering, No deformation
Deb. 5: Very-fast	Severe blistering, Severe deformation	Minor blistering, No deformation	

debinding regime 2 was further adopted. It is nevertheless confirmed that for low ceramic loadings, the debinding process must be slow. With higher loadings, the debinding time can be significantly reduced from 35 to ~10 – 16 hours. Therefore, optimizing the ceramic loading allows us to limit energy consumption while ensuring the successful removal of binders.

### 3.4. Shrinkage and densification

The selection of an appropriate sintering regime is crucial for achieving desired properties and quality in the final sintered products. Based on the results of the optical dilatometer (selected images in Fig. S2), sintering temperatures between 1200 – 1350 °C (with steps of 50 °C) were chosen for further analysis. Fig. 10 (a-c) reports the shrinkage of the 3D printed components in the planar (x, y) and axial (z) directions at different sintering temperatures. Note that the shrinkage is consistent in the planar directions, but lower in the axial direction. Typically, printed components show higher shrinkage in the axial direction due to weak interlayer binding [53]. Results are consistent with what reported by Liu *et al.* and interpreted as excellent bonding between the layers [54]. The shrinkage increases linearly in the selected temperature range, apart from an abrupt increase in the slope of the curve between 1250 °C and 1300 °C: this corresponds to a significant increase in the relative density (see Fig. 10(d)). As the ceramic content in the filaments increases, the shrinkage of the printed parts decreases, and their relative density increases. In fact, higher ceramic loadings result in denser packing of particles in the green parts. The rearrangement and compaction of the particles is less pronounced (lower shrinkage), and the densification is higher. However, when comparing the density of F80 samples to uniaxially powder pressed discs sintered at the same temperatures, the printed samples exhibited significantly lower densities, probably due to the residual porosity from the binder removal process. The measured x,y shrinkage at 1350 °C was in good agreement with the

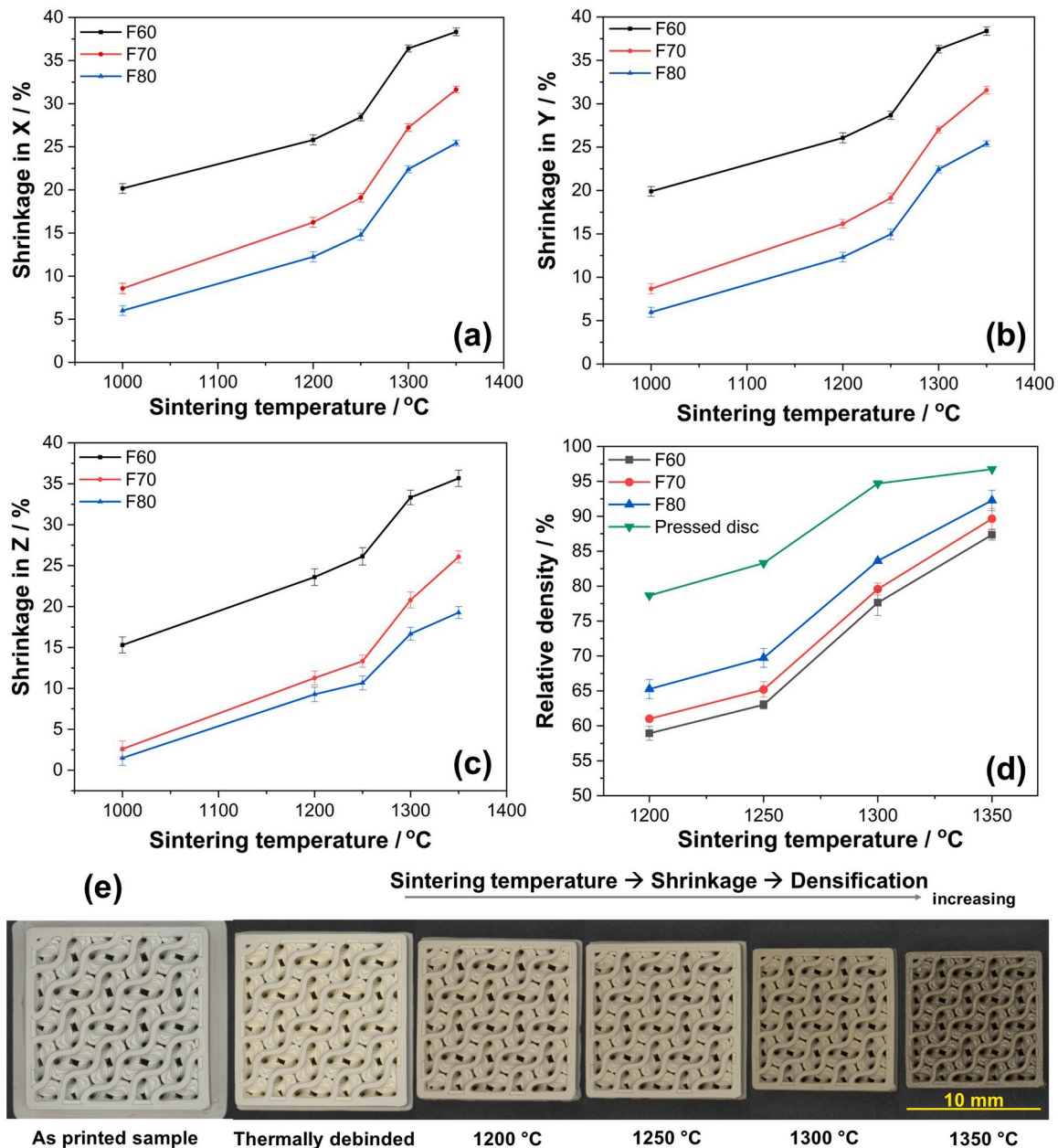


Fig. 10. Variation of shrinkage in the (a) x-direction (b) y-direction (c) z-direction as a function of the sintering temperature. Measurements were taken with a digital caliper. (d) Evolution of the relative density with the sintering temperature of additively manufactured and sintered gyroidal components. (e) Optical images of the sintered samples printed with F70.

theoretical shrinkage values calculated assuming material isotropy and full densification (see Table S2); axial anisotropy and incomplete densification found expression in the lower shrinkage measured in the z direction. The geometrical evolution of the sintered BaTiO<sub>3</sub> samples (F70) is accompanied by a change in color from white to pale yellow, as depicted in Fig. 10(e).

Side views and fracture surfaces of the sintered samples shown in Fig. 10(e) are reported in Fig. S7 as they offer significant insights about the bonding between the layers and its evolution with the sintering temperature. Layer bonding appears excellent both on the surface (Fig. S7(a-d)) and within the section (Fig. S7(e-l)). The fracture surface (Fig. S7(i-l)) appears rough in the samples sintered at 1200 °C and 1250 °C due to the presence of pores; it becomes smoother for sintering temperature increasing to 1300 °C due to higher densification and small grain size [55]. Finally, when the temperature further increases to 1350 °C, the surface becomes again rough due to grain growth.

### 3.5. Microstructural and porosimetry analysis

The microstructure of samples fabricated using F60, F70, F80 and sintered at different temperatures are shown in Fig. 11. In addition, the evolution of grain size with temperature is reported in Fig. 12.

Large micron-sized and interconnected voids can be clearly observed in samples sintered at lower temperatures (1200 °C and 1250 °C). They are the result of binder removal and cannot be removed at such low sintering temperatures. The grain size (rather the particle size) remains almost unaffected; however, necking could be clearly observed among the particles denoting the initial stages of necking. When the temperature increases to 1300 °C, mass transport is significantly enhanced and the residual porosity is significantly reduced due to continuous neck growth. Also, the pores become more isolated with enhanced densification. Nevertheless, the grain size remains rather constant. However, further increasing the temperature to 1350 °C, abnormal grain growth is

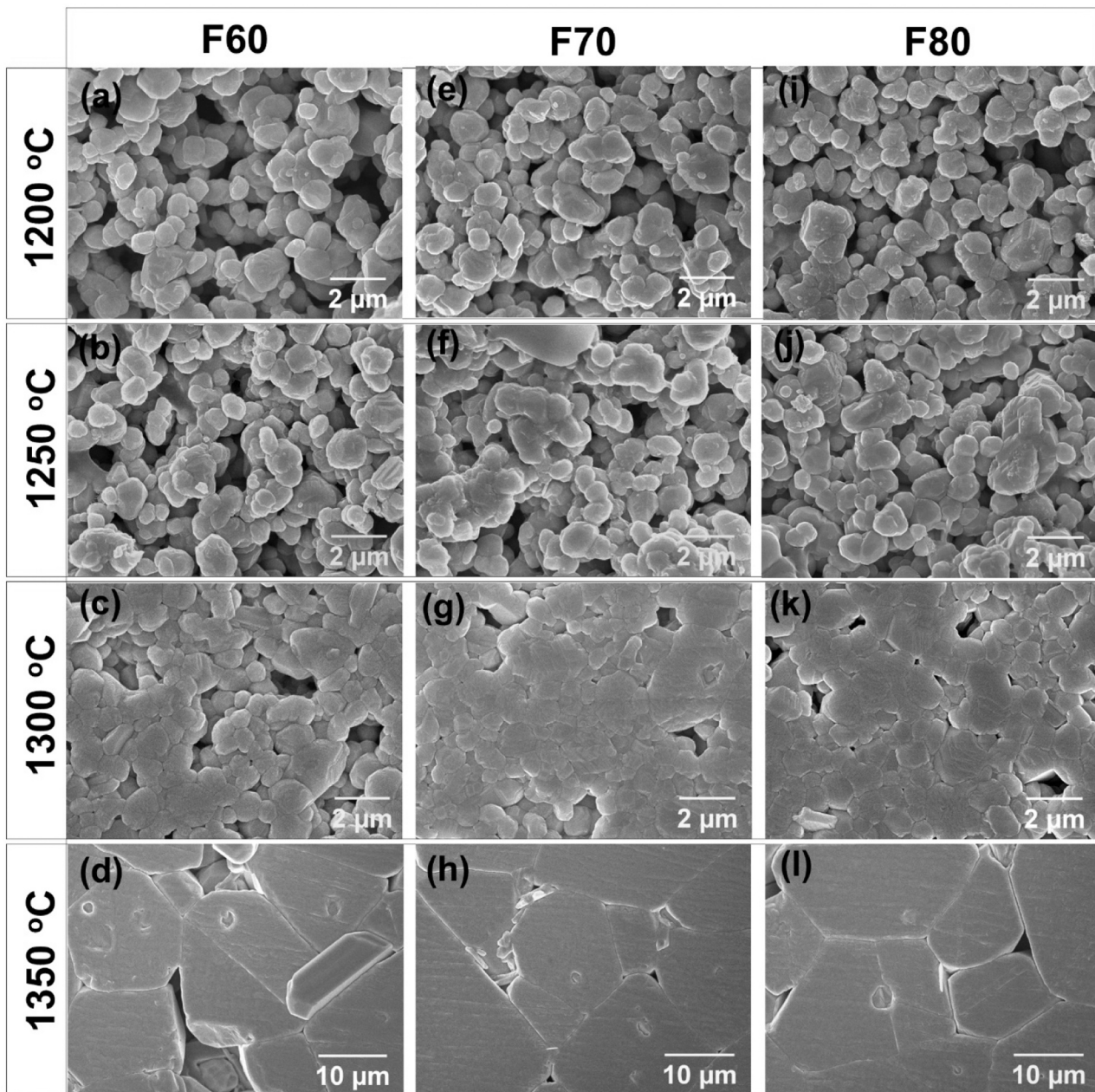


**Fig. 11.** SEM micrographs of sintered samples at different temperatures ranging from 1200 °C to 1350 °C (in steps of 50 °C) for samples fabricated with (a-d) F60 (e-h) F70 (i-l) F80. Kindly note that samples sintered at 1300 °C and 1350 °C were only polished and thermally etched.

induced, with grains reaching dimensions  $>20 \mu\text{m}$ , due to strongly enhanced material transport conditions. Therefore, between these two temperatures there is a certain threshold above which abnormal grain growth occurs, according to previously reported literature [56]. An additional sintering treatment was performed at 1325 °C to determine the threshold temperature for abnormal grain growth. Indeed, it resulted in a bimodal distribution of small and large grain sizes, indicating grain growth through Ostwald ripening (Fig. S8). The ICP chemical analysis (Fig. S1(d)) indicated that the starting powder has an atomic ratio of Ba/Ti less than 1; suggesting that Ti-rich  $\text{BaTiO}_3$  was used. The excess  $\text{TiO}_2$  can react with  $\text{BaTiO}_3$  to form a eutectic liquid phase ( $\text{Ba}_6\text{Ti}_{17}\text{O}_{40}$ ), which is believed to be the cause for inducing abnormal grain growth [57,58].

SEM analysis was combined with mercury porosimetry to obtain a more comprehensive understanding of the porosity and density of the samples. An overview of the SEM micrographs for printed and pressed

samples sintered at 1300 °C is shown in Fig. S9 to better correlate with the porosimetry results. Fig. 13 reports the cumulative pore volume and the pore size distribution of the printed samples sintered at 1300 °C and 1350 °C, together with a powder pressed disc sintered at 1300 °C. Density values calculated from mercury porosimetry data are slightly lower than those measured following Archimedes principle and tend to get closer (4 % deviation) for higher sintering temperatures and solid loadings. Nevertheless, the analysis confirms the observed trends from shrinkage and density assessment: the cumulative pore volume and the pore size decrease with increasing temperature and increasing ceramic loading.

Pore size in the range of 0.1 – 5  $\mu\text{m}$  is attributed to the binder burn out process. In fact, powder-pressed disc only exhibits smaller pores (0.02 – 0.1  $\mu\text{m}$ ), which is also present in F60, F70, and F80 samples and is attributed to particle packing behavior. Only the combination of the highest ceramic loading (F80) and the sintering temperature (1350 °C)

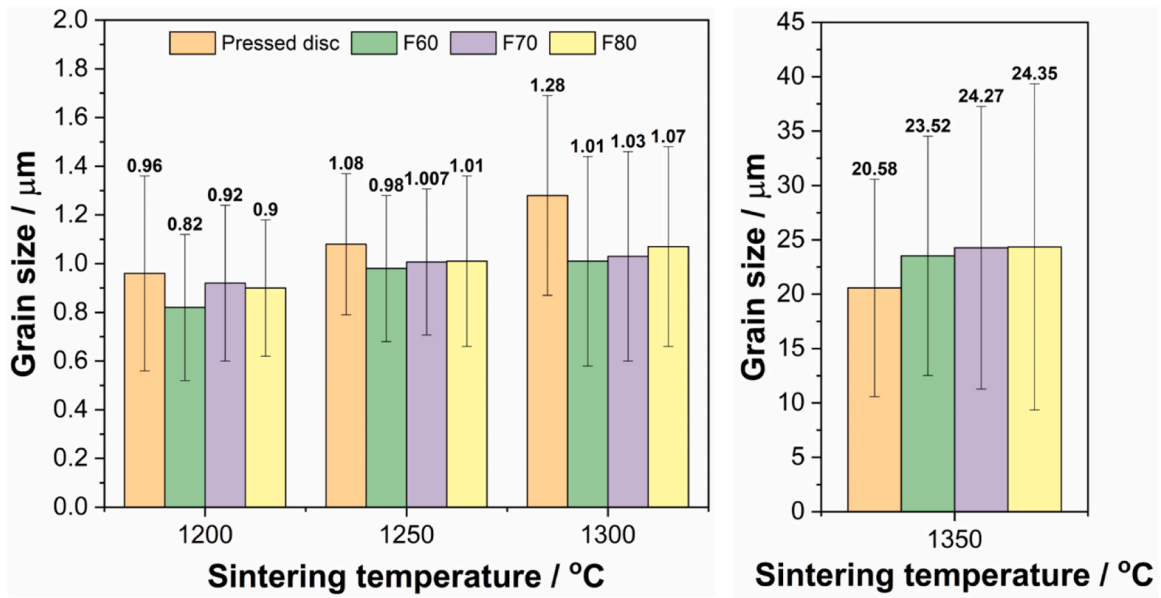


Fig. 12.. Evolution of the grain size as a function of the sintering temperature and ceramic loading. This analysis was performed on the porous prisms with 25 % infill density (see Table 1).

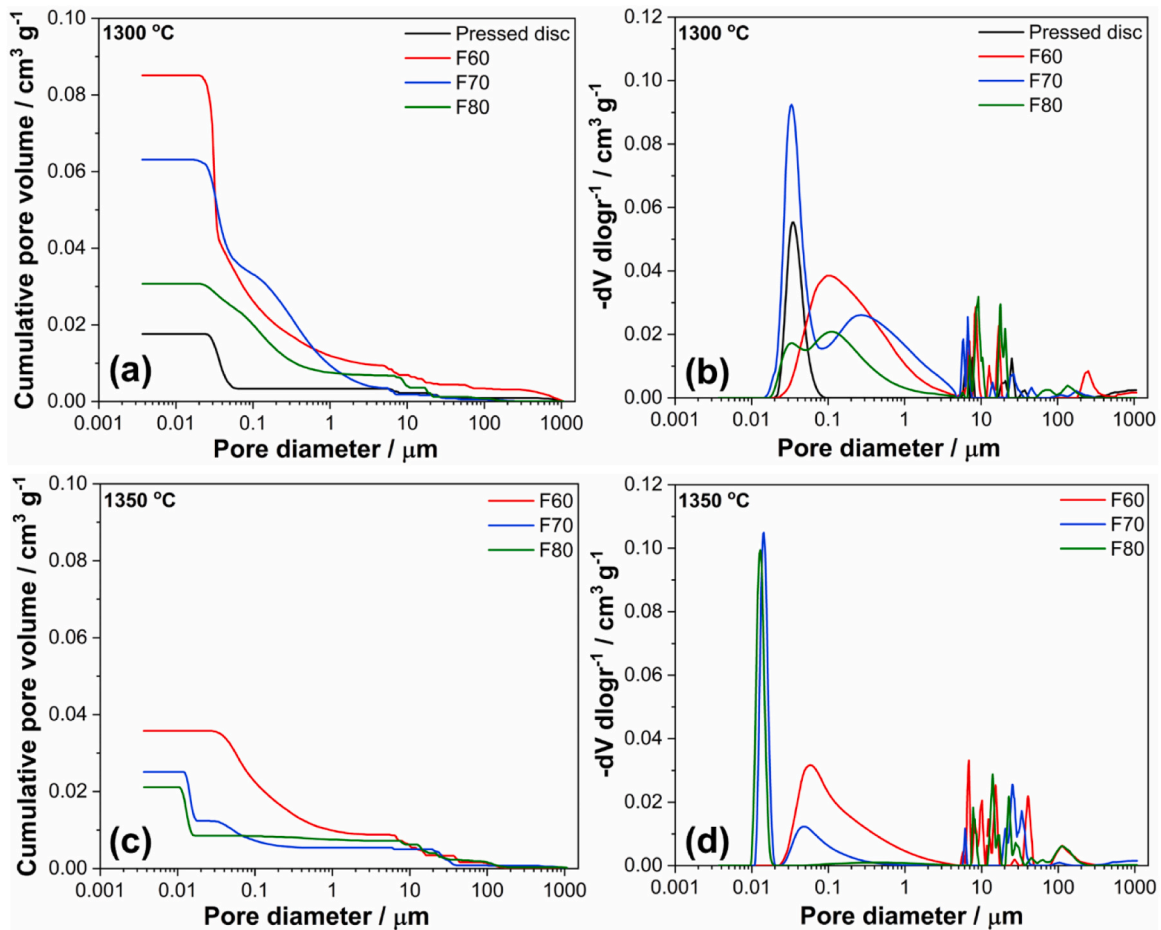


Fig. 13.. Mercury intrusion porosimetry of the sintered samples: (a, c) cumulative pore volume (b, d) pore size distribution of the additively manufactured and sintered samples. Only the gyroidal samples were assessed for such measurements. For comparison, an uniaxially powder pressed disc was sintered at 1300 °C for the measurement.

allows elimination of the pores left by the binder, but at the expense of the grain size. Pores larger than 4  $\mu\text{m}$  appear randomly and are attributed to air pockets (Fig. S7) and structural defects. Air pockets within the powder can occur during the synthesis or handling of the material and can persist throughout subsequent processing steps. Structural defects may also originate from the manufacturing process (e.g., the starting point of each layer often leaves an open pore, etc.) [59].

### 3.6. XRD and Raman analysis

Further characterization was carried on only on samples produced with F70, as it represents the best compromise between ceramic loading and printability. X-ray diffraction (XRD) and Raman analysis provide valuable insights into the crystallographic structure and allow phase identification of the materials. Fig. 14(a) displays the XRD patterns of both, the as-received BaTiO<sub>3</sub> powders and the ceramics sintered at different temperatures. XRD analysis reveals that all sintered ceramic samples exhibit phase pure BaTiO<sub>3</sub> (JCPDS: 00–005–0626). There are no reflections of secondary phases present. These findings are in good agreement with the Raman analysis (depicted in Fig. 14(b); Raman active modes at 258  $\text{cm}^{-1}$ , 305  $\text{cm}^{-1}$ , 514  $\text{cm}^{-1}$ , 719  $\text{cm}^{-1}$  represent the Raman shift of polycrystalline tetragonal barium titanate [55]). As the sintering temperature increased to 1350  $^{\circ}\text{C}$ , there was clear evidence of the reflection splitting of (002) and (200) at  $2\theta \sim 45^{\circ}$ , indicating that tetragonality increases with sintering temperature [56]. The sintered BaTiO<sub>3</sub> ceramics had the highest tetragonality (c/a ratio) at 1350  $^{\circ}\text{C}$  with very big grains, as depicted in Fig. 15(b).

A quantitative analysis of the diffraction data reveals significant changes of the lattice parameters for different sintering temperatures (Fig. 15(a)). Especially for samples sintered at 1350  $^{\circ}\text{C}$  with large grain sizes (see Fig. 12), the unit cell parameters show a discontinuous behavior: the a-axis becomes smaller, while the c-axis shows a pronounced increase in comparison to lower sintering temperatures. From the unit cell parameters, the unit cell distortion  $\eta_T$  can be calculated as:

$$\eta_T = c_T/a_T - 1 \quad (5)$$

Fig. 15(b) shows the values of  $\eta_T$  for the investigated samples. As anticipated, the sample with large grains shows a discontinuous behavior and an extraordinarily high  $\eta_T$ , which correspond to a higher tetragonality in the sample. There is a clear correlation between unit cell distortion and grain size: in fact, small grain sizes correspond to small domain sizes and many intergranular constraints, which give rise to increased stresses hindering the transition to tetragonal phase; bigger grains, on the other hand, pose less constraints to phase transitions and thus allow an increased unit cell distortion [60,61]. Since the latter is

directly linked with the electromechanical and dielectric parameters, the best performance is anticipated for said sample; hence, investigation of the electromechanical and dielectric properties will focus only on samples sintered at 1350  $^{\circ}\text{C}$ .

### 3.7. Dielectric and piezoelectric properties

When considering the dielectric and piezoelectric properties, both the grain size and the density play a crucial role in determining the overall performance of a material [62]. In this study, the samples with a relative density of approximately 90 % were used for such functional characterization. Fig. 16(a) shows the frequency dependence of the dielectric constant and dielectric loss ( $\tan \delta$ ) of printed and sintered BaTiO<sub>3</sub> (sintered at 1350  $^{\circ}\text{C}$ ) disc at room temperature. The optical image of the sintered disc is reported in Fig. S10. There is a gradual decrease in the permittivity value as a function of frequency. Similar trends were also observed for the dielectric loss. The values for permittivity and  $\tan \delta$  measured at 1 kHz are reported in Table 4, which is comparable to the previously reported values. Careful observations reveal that there is a slight increase in the dielectric properties with increasing solid loadings in the measured samples (from F70 to the conventional sintered disc). Materials with low porosity (high solid loadings) tends to exhibit a denser microstructure with higher dielectric, piezoelectric and ferroelectric properties [63].

Fig. 16(b-d) exhibits the hysteresis loops (at room temperature) of the piezoelectric coefficient  $d_{33}$ , polarization, and strain of the additively manufactured and powder pressed disc samples sintered at 1350  $^{\circ}\text{C}$ . The relevant electromechanical properties are summarized in Table 4. When considering the hysteresis loops, both the remanent and saturation values are important and depend on specific application requirements. The remanent value is vital if preserving a certain polarization state is necessary, while the saturation value is critical for establishing a robust piezoelectric response under high electric fields. The electric-field-dependent polarization hystereses are fully developed by reaching the saturation values and the samples exhibit high ferroelectric properties. The values in Table 4 suggest that the saturation polarization increases from 11.39  $\mu\text{C cm}^{-2}$  to 12.33  $\mu\text{C cm}^{-2}$ , on increasing the solid loadings (F70 to F80) in the sintered samples. Similar trends were observed for the remanent polarization. The electric field-dependent strain hystereses are typical for ferroelectric materials. The hystereses are very symmetric with maximum strains of 0.053 % for F80 and 0.041 % for F70. The strain these materials display is indicative of their efficiency in transforming electrical energy into mechanical energy. Often, higher strain values are desired for better performance. The maximum piezoelectric charge coefficient of 222  $\text{pC N}^{-1}$  was

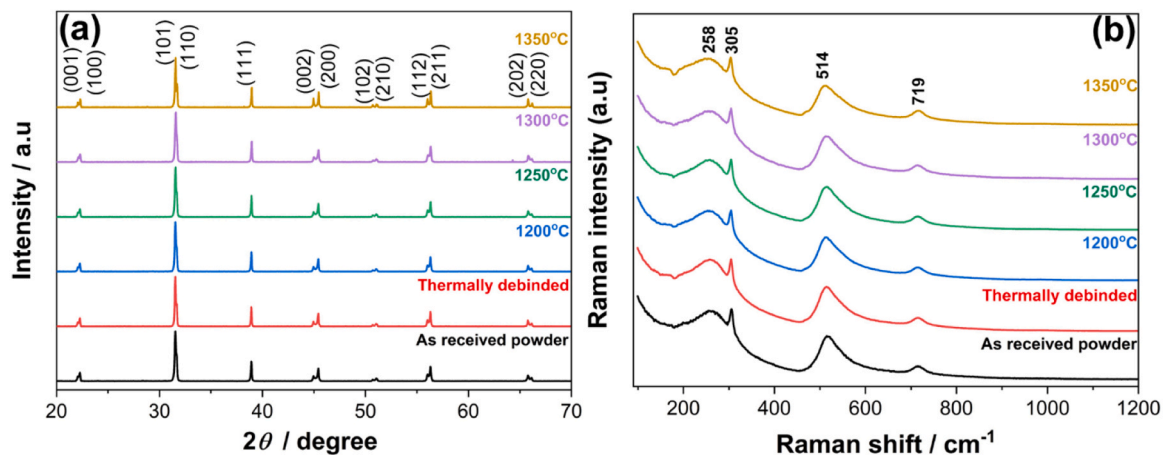


Fig. 14.. (a) X-ray diffraction (XRD) and (b) Raman spectroscopy of the sintered samples at different temperatures. The measurements were carried out on the as received powders and on porous prisms produced with filament F70.

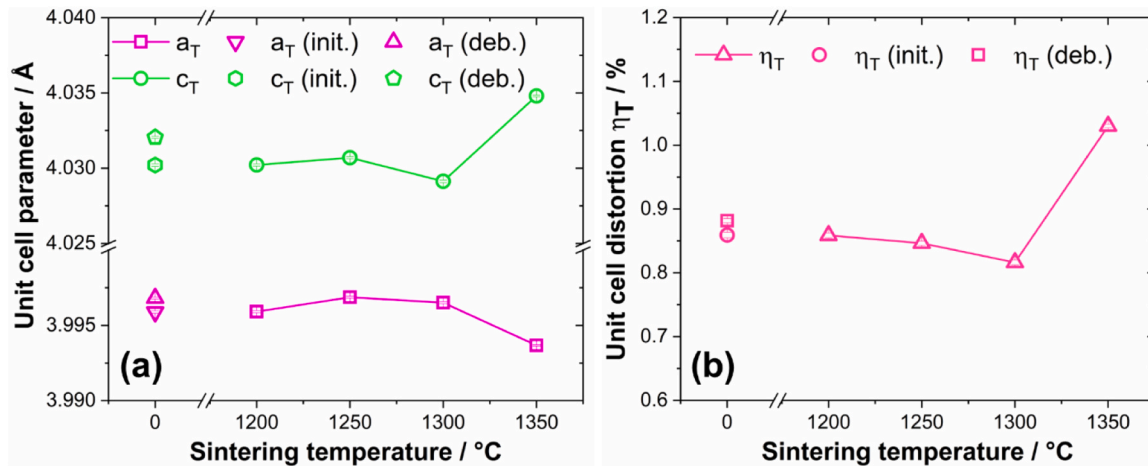


Fig. 15.. (a) Unit cell parameters and (b) unit cell distortions for the initial powder and the debinded samples as well as for the sintered samples as a function of sintering temperature. This analysis has been carried out on the porous prisms printed with filament F70. (Here init. refers to the initial BaTiO<sub>3</sub> powder and deb. refers to the thermally debinded powder).

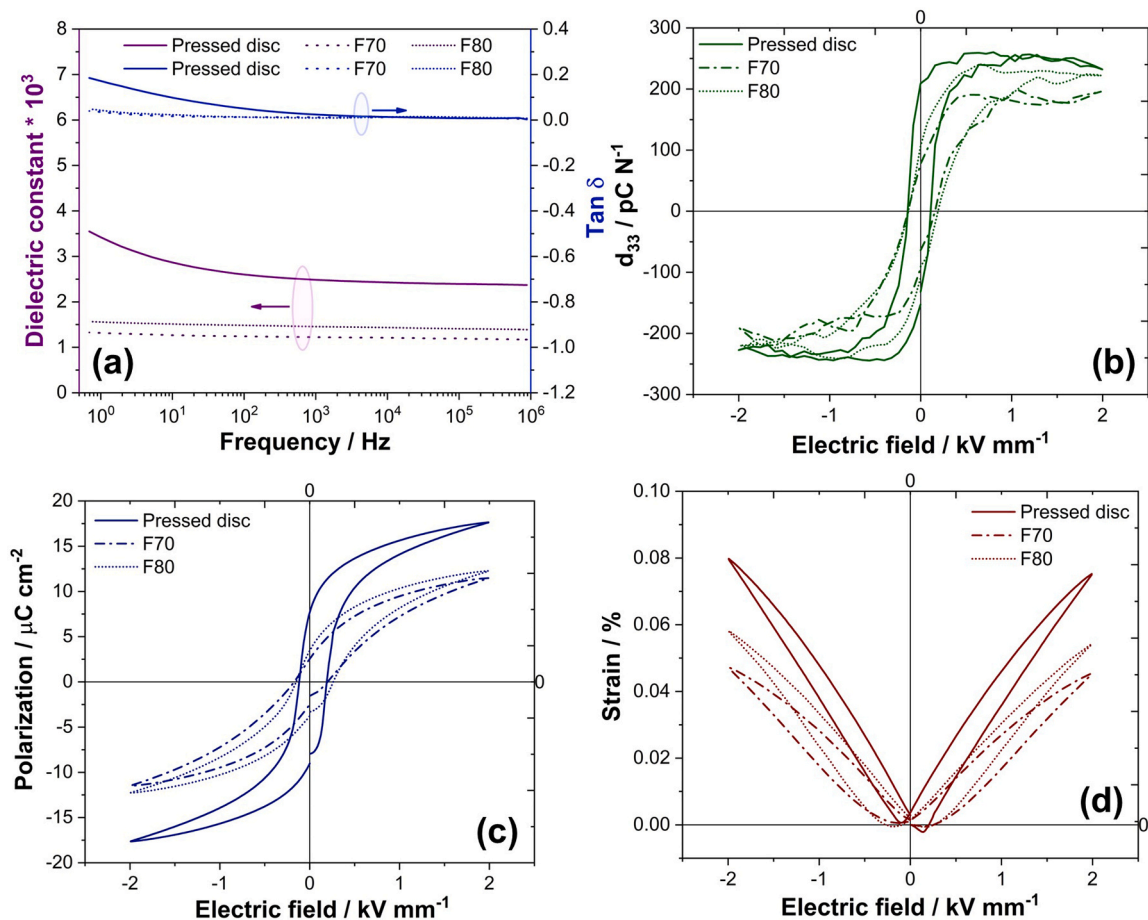


Fig. 16.. (a) Dielectric constant and loss factor as a function of frequency at room temperature. Electromechanical properties: Variation of (b) piezoelectric coefficient,  $d_{33}$ ; (c) polarization,  $P$ ; (d) strain,  $S$  with electric field. All the measurements were taken on the 3D printed discs sintered at 1350 °C for 2 hours.

displayed by a sample fabricated with F80. However, on decreasing the solid loadings, the  $d_{33\max}$  decreases to 196 pC N<sup>-1</sup>. Even the  $d_{33\text{rem}}$  showed similar tendencies. It is important to point out that better properties are achieved with higher solid loadings, with obvious reason as discussed in the above paragraph. However, there isn't a disqualifying and noticeably huge difference between the properties of the samples fabricated using F70 or F80.

The piezoelectric, ferroelectric, and dielectric characteristics of our printed material are within the range of values that are typically reported for BaTiO<sub>3</sub> produced traditionally or by using other 3D printing techniques (Table 4). In contrast to the properties exhibited by the powder pressed disc, the observed properties for the printed components are significantly lower. The reason for such deterioration in the properties of the additively manufactured components is due to the presence

**Table 4**Dielectric and ferroelectric properties of the printed BaTiO<sub>3</sub> samples in our study and previously reported literature.

Fabrication method	Relative density (%)	$\epsilon$ (1 kHz)	Tan $\delta$ (1 kHz)	$d_{33\max}$ (pC N <sup>-1</sup> )	$P_{\max}$ ( $\mu\text{C cm}^{-2}$ )	$S_{\max}$ (%)	Ref.
Powder pressed pellet	96	2501	0.023	242	17.65	0.075	This work
FFF_70	88	1228	0.010	196	11.39	0.041	
FFF_80	92	1472	0.012	221	12.33	0.053	
Stereolithography	93.7	1350	0.012	160	~ 10	–	[64]
Binder jetting	65.2	~ 620	~ 0.01	74.1	–	–	[18]
DLP	95.4	1543	0.0185	180	~ 20	–	[65]

of residual porosity from the binder burn out. This is well supported by the density and mercury porosimetry measurements (Fig. 10(d), Fig. 13). In addition to this, the printing defects cannot be ignored completely, as shown in Fig. S11. Such defects give rise to additional porosity in the sample, thus lowering down the properties. Even though the properties exhibited by our printed components are in good agreement to already reported values, yet better properties can be further achieved with optimized printing strategy and sintering profiles.

#### 4. Conclusion

This work demonstrates the feasibility of fabricating composite filaments of undoped BaTiO<sub>3</sub> with various ceramic loadings which can be used by a wide range of inexpensive FFF printers. The filaments were thoroughly characterized to ensure selection of “trouble free” filament composition for extrusion and printing. The fabricated filaments can be printed with nozzles down to 0.3 mm diameter. Complex porous structures as well dense pellets were printed, debinded and sintered. A single step thermal debinding was employed for the porous structures, while dense pellets had to undergo an additional chemical debinding step prior to thermal debinding and sintering. With optimized debinding and sintering regimes, no defects or cracks were observed. Samples sintered at 1350 °C exhibited dense microstructures with coarse grains. In addition, the dielectric and ferroelectric properties of the sintered components were in good agreement in comparison to previously reported values. This straightforward and low-cost material extrusion process can be further exploited to print functional structures, in contrast to the costly equipment or the precise control of the rheology for the feedstock required for other AM technologies.

#### CRediT authorship contribution statement

**Giorgia Franchin:** Writing – review & editing, Supervision, Resources, Methodology, Conceptualization. **Marián Janek:** Writing – review & editing, Supervision, Resources, Funding acquisition, Conceptualization. **Manuel Hinterstein:** Writing – review & editing, Validation, Funding acquisition. **Luboš Bača:** Writing – review & editing, Validation, Funding acquisition. **Zora Hajdúchová:** Investigation. **Zdenko Špitalský:** Investigation. **Subhadip Bhandari:** Writing – original draft, Visualization, Investigation, Funding acquisition, Formal analysis, Data curation. **Peter Veteška:** Writing – review & editing, Validation, Investigation. **Gaurav Vajpayee:** Investigation, Funding acquisition.

#### Declaration of Competing Interest

The authors declare the following financial interests/personal relationships which may be considered as potential competing interests. Subhadip Bhandari reports financial support was provided by Foundation of the Savings Bank of Padua and Rovigo. Subhadip Bhandari reports financial support was provided by Ministry of Education Science Research and Sport of the Slovak Republic. Manuel Hinterstein, Gaurav Vajpayee reports financial support was provided by Fraunhofer Institute for Mechanics of Materials IWM. Marián Janek and Zdenko Špitalský reports financial support was provided by Slovak Grant Agency VEGA.

Luboš Bača reports financial support was provided by European Regional Development Fund. Giorgia Franchin reports article publishing charges was provided by University of Padua. If there are other authors, they declare that they have no known competing financial interests or personal relationships that could have appeared to influence the work reported in this paper

#### Data Availability

Data will be made available on request.

#### Acknowledgement

Subhadip Bhandari gratefully acknowledges the CARIPARO Foundation, Padova, Italy, for his Ph.D. scholarship. Additionally, the funding from National Scholarship Programme of the Slovak republic (NSP SAIA ID: 38701) is highly acknowledged for the research stay at the Slovak University of Technology in Bratislava. The authors acknowledge Dr. Jozef Feranc for the rheological measurements, Dr. Katarína Tománová for SEM analysis, Dr. Matúš Zemlička for mercury porosimetry measurements, Dr. Tibor Dubaj for TGA measurements, and Dr. Lukáš Gál for the Raman analysis. Manuel Hinterstein and Gaurav Vajpayee thank the Fraunhofer Internal Programs for financial support under grant no. Attract 40-04857. The financial support of Slovak Grant Agency VEGA (grant No. VEGA 1/0070/22, 1/0342/21, 2/0056/24) and the project “Advancing University Capacity and Competence in Research, Development and Innovation”(ITMS project code: 313021×329) supported by Slovak Operational Programme Integrated Infrastructure and funded by the European Regional Development Fund are also gratefully acknowledged.

#### Appendix A. Supporting information

Supplementary data associated with this article can be found in the online version at [doi:10.1016/j.addma.2024.104238](https://doi.org/10.1016/j.addma.2024.104238).

#### References

- [1] C. Chen, X. Wang, Y. Wang, D. Yang, F. Yao, W. Zhang, B. Wang, G.A. Sewvandi, D. Yang, D. Hu, Additive manufacturing of piezoelectric materials, *Adv. Funct. Mater.* 30 (2020) 2005141.
- [2] P.K. Panda, B. Sahoo, PZT to Lead free piezo ceramics: a review, [http://dx. Doi. Org. /10. 1080/00150193. 2015. 997146](http://dx.doi.org/10.1080/00150193.2015.997146) 474 (2015) 128.
- [3] B. Tiwari, T. Babu, R.N.P. Choudhary, Piezoelectric lead zirconate titanate as an energy material: a review study, *Mater. Today Proc.* 43 (2021) 407.
- [4] Y. Li, K.S. Moon, C.P. Wong, Materials science. electronics without lead, *Science* 308 (2005) 1419.
- [5] S.J.S. Flora, G. Flora, G. Saxena, Environmental occurrence, health effects and management of lead poisoning, *Lead. Chem. Anal. Asp. Environ. Impact Heal. Eff.* (2006) 158.
- [6] M. Acosta, N. Novak, V. Rojas, S. Patel, R. Vaish, J. Koruza, G.A. Rossetti, J. Rödel, BaTiO<sub>3</sub>-based piezoelectrics: fundamentals, current status, and perspectives, *Appl. Phys. Rev.* 4 (2017).
- [7] M. Özen, M. Mertens, F. Snijkers, G. Van Tendeloo, P. Cool, Texturing of Hydrothermally Synthesized BaTiO<sub>3</sub> in a strong magnetic field by slip casting, *Ceram. Int.* 42 (2016) 5382.
- [8] J.F. Fernández, P. Durán, C. Moure, Microstructure development of tape casting BaTiO<sub>3</sub> ceramics, [http://dx. Doi. Org. /10. 1080/00150199208223348](http://dx.doi.org/10.1080/00150199208223348) 127 (2011) 65.
- [9] L. Zhang, J. Zhai, X. Yao, Dielectric properties of electrophoretically deposited and isothermally pressed BaTiO<sub>3</sub> thick films, *J. Am. Ceram. Soc.* 91 (2008) 2075.

- [10] I. Stanimirović, Z. Stanimirović, Piezoelectric ceramics by powder injection molding, 27th Int. Conf. Microelectron. MIEL 2010 - Proc. 231 (2010) 2010.
- [11] Y. Ohara, K. Koumoto, H. Yanagida, Effect of crystal-axis orientation on dielectric properties of ceramics prepared from fibrous barium titanate, *J. Am. Ceram. Soc.* 77 (1994) 2327.
- [12] A. Zocca, P. Colombo, C.M. Gomes, J. Günster, Additive manufacturing of ceramics: issues, potentialities, and opportunities, *J. Am. Ceram. Soc.* 98 (2015) 1983.
- [13] C.A. Goat, R.W. Whatmore, The Effect of grinding conditions on lead zirconate titanate machinability, *J. Eur. Ceram. Soc.* 19 (1999) 1311.
- [14] Z. Chen, Z. Li, J. Li, C. Liu, C. Lao, Y. Fu, C. Liu, Y. Li, P. Wang, Y. He, 3D Printing of ceramics: a review, *J. Eur. Ceram. Soc.* 39 (2019) 661.
- [15] Y. Lakhdar, C. Tuck, J. Binner, A. Terry, R. Goodridge, Additive manufacturing of advanced ceramic materials, *Prog. Mater. Sci.* 116 (2021) 100736.
- [16] M.H. Carrillo, G. Lee, C. Maniere, E.A. Olevsky, Additive manufacturing of powder components based on subtractive sintering approach, *Rapid Prototyp. J.* 27 (2021) 1731.
- [17] I. Gibson, D. Rosen, B. Stucker, M. Khorasani, D. Rosen, *Addit. Manuf. Technol.* (2021).
- [18] S.M. Gaytan, M.A. Cadena, H. Karim, D. Delfin, Y. Lin, D. Espalin, E. MacDonald, R. B. Wicker, Fabrication of barium titanate by binder jetting additive manufacturing technology, *Ceram. Int.* 41 (2015) 6610.
- [19] G. Ding, R. He, K. Zhang, C. Xie, M. Wang, Y. Yang, D. Fang, Stereolithography-based additive manufacturing of gray-colored sic ceramic green body, *J. Am. Ceram. Soc.* 102 (2019) 7198.
- [20] Y. Liu, L. Zhan, L. Wen, L. Cheng, Y. He, B. Xu, Q. Wu, S. Liu, Effects of Particle Size and Color on Photocuring Performance of Si3N4 Ceramic Slurry by Stereolithography, *J. Eur. Ceram. Soc.* 41 (2021) 2386.
- [21] J.H. Jang, S. Wang, S.M. Pilgrim, W.A. Schulze, Preparation and Characterization of Barium Titanate Suspensions for Stereolithography, *J. Am. Ceram. Soc.* 83 (2000) 1804.
- [22] J. Abel, U. Scheithauer, T. Janics, S. Hampel, S. Cano, A. Müller-Köhn, A. Günther, C. Kukla, T. Moritz, Fused Filament Fabrication (FFF) of Metal-Ceramic Components, *JoVE (J. Vis. Exp.* 2019 (2019) e57693.
- [23] L. del-Mazo-Barbara, M.P. Ginebra, Rheological Characterisation of Ceramic Inks for 3D Direct Ink Writing: A Review, *J. Eur. Ceram. Soc.* 41 (2021) 18.
- [24] A. Hadian, L. Koch, P. Koberg, F. Sarraf, A. Liersch, T. Sebastian, F. Clemens, Material Extrusion Based Additive Manufacturing of Large Zirconia Structures Using Filaments with Ethylene Vinyl Acetate Based Binder Composition, *Addit. Manuf.* 47 (2021) 102227.
- [25] F. Castles, D. Isakov, A. Lui, Q. Lei, C.E.J. Dancer, Y. Wang, J.M. Janurudin, S. C. Speller, C.R.M. Groveron, P.S. Grant, Microwave Dielectric Characterisation of 3D-Printed BaTiO<sub>3</sub>/ABS Polymer Composites, *Sci. Rep.* 6 (1) (2016).
- [26] P. Parsons, Z. Larimore, M. Mirotznik, G. Mitchell, Composite Materials Development for Fused Filament Fabrication of RF Systems, *Appl. Comput. Electromagn. Soc. J.* 35 (2020) 1278.
- [27] S. Alexandridis and A.M. Rimašauskas, *Fabrication and Characterization of PVDF/BaTiO<sub>3</sub> 3D Printing Material Master's Final Degree Project*, (2022).
- [28] H. Kim, J. Johnson, L.A. Chavez, C.A. Garcia Rosales, T.L.B. Tseng, Y. Lin, Enhanced Dielectric Properties of Three Phase Dielectric MWCNTs/BaTiO<sub>3</sub>/PVDF Nanocomposites for Energy Storage Using Fused Deposition Modeling 3D Printing, *Ceram. Int.* 44 (2018) 9037.
- [29] R. Colella, F.P. Chietera, A. Greco, F. Montagna, L. Catarinucci, 3D-Printed Tunable UHF RFID PIFA Realized with BaTiO<sub>3</sub>Enhanced PLA for Multipurpose Applications, 2020 33rd Gen. Assem. Sci. Symp. Int. Union Radio Sci. URSI GASS 2020 (2020) 2020.
- [30] Y. Wu, D. Isakov, P.S. Grant, Fabrication of Composite Filaments with High Dielectric Permittivity for Fused Deposition 3D Printing, *Mater. (Basel)* 10 (2017).
- [31] B. Khatri, K. Lappe, M. Hadedank, T. Mueller, C. Megnin, T. Hanemann, Fused Deposition Modeling of ABS-Barium Titanate Composites: A Simple Route towards Tailored Dielectric Devices, *Polym. (Basel)* 10 (2018).
- [32] A. Dey, I.N.R. Eagle, N. Yodo, A Review on Filament Materials for Fused Filament Fabrication, *J. Manuf. Mater. Process.* 5 (2021).
- [33] M.R. Ismael, F. Clemens, T. Graule, M.J. Hoffmann, Effects of Different Thermoplastic Binders on the Processability of Feedstocks for Ceramic Co-Extrusion Process, *Ceram. Int.* 37 (2011) 3173.
- [34] A. Hadian, M. Fricke, A. Liersch, F. Clemens, Material Extrusion Additive Manufacturing of Zirconia Parts Using Powder Injection Molding Feedstock Compositions, *Addit. Manuf.* 57 (2022) 102966.
- [35] T. Heim, F. Kern, Influence of the Feedstock Preparation on the Properties of Highly Filled Alumina Green-Body and Sintered Parts Produced by Fused Deposition of Ceramic, 241, *Ceram 2023 Vol. 6* (6) (2023) 241–254, 241.
- [36] M. Orlovská, M. Hain, M. Kitzmantel, P. Veteška, Z. Hajdúchová, M. Janek, M. Vozárová, and Bača, *Monitoring of Critical Processing Steps during the Production of High Dense 3D Alumina Parts Using Fused Filament Fabrication Technology*, *Addit. Manuf.* 48 (2021).
- [37] T. Sebastian, M. Bach, A. Geiger, T. Lusiola, L. Kozielski, F. Clemens, Investigation of Electromechanical Properties on 3D Printed Piezoelectric Composite Scaffold Structures, *Mater. (Basel)* 14 (2021).
- [38] P. Veteška, Z. Hajdúchová, J. Feranc, K. Tomanová, J. Milde, M. Kritikos, L. Bača, M. Janek, Novel Composite Filament Usable in Low-Cost 3D Printers for Fabrication of Complex Ceramic Shapes, *Appl. Mater. Today* 22 (2021).
- [39] M. Vozárová, et al., Preparation of Fully Dense Boron Carbide Ceramics by Fused Filament Fabrication (FFF), *J. Eur. Ceram. Soc.* 43 (2023) 1751.
- [40] M. Janek, et al., Mechanical Testing of Hydroxyapatite Filaments for Tissue Scaffolds Preparation by Fused Deposition of Ceramics, *J. Eur. Ceram. Soc.* 40 (2020) 4932.
- [41] I. Özden, A. Iveković, A. Kocjan, Additive Manufacturing of Ceramics from Thermoplastic Feedstocks, *Open Ceram.* 6 (2021).
- [42] N.K. Bankapalli, V. Gupta, P. Saxena, A. Bajpai, C. Lahoda, J. Polte, Filament Fabrication and Subsequent Additive Manufacturing, Debinding, and Sintering for Extrusion-Based Metal Additive Manufacturing and Their Applications: A Review, *Compos. Part B Eng.* 264 (2023) 110915.
- [43] Z. Lotfizarei, A. Mostafapour, A. Barari, A. Jalili, A.E. Patterson, Overview of Debinding Methods for Parts Manufactured Using Powder Material Extrusion, *Addit. Manuf.* 61 (2023) 103335.
- [44] C.A. Schneider, W.S. Rasband, K.W. Eliceiri, NIH Image to ImageJ: 25 Years of Image Analysis, *Nat. Methods* 2012 97 (9) (2012) 671.
- [45] J.J. Fallon, S.H. McKnight, M.J. Bortner, Highly Loaded Fiber Filled Polymers for Material Extrusion: A Review of Current Understanding, *Addit. Manuf.* 30 (2019) 100810.
- [46] N. Venkataraman, S. Rangarajan, M.J. Matthewson, B. Harper, A. Safari, S. C. Danforth, G. Wu, N. Langrana, S. Guceri, A. Yardimci, Feedstock Material Property - Process Relationships in Fused Deposition of Ceramics (FDC), *Rapid Prototyp. J.* 6 (2000) 244.
- [47] B.N. Turner, R. Strong, S.A. Gold, A Review of Melt Extrusion Additive Manufacturing Processes: I. Process Design and Modeling, *Rapid Prototyp. J.* 20 (2014) 192.
- [48] S.N.A.M. Halidi, J. Abdullah, Moisture Effects on the ABS Used for Fused Deposition Modeling Rapid Prototyping Machine, *IEEE Symp. Humanit. Sci. Eng. Res.* 2012 (2012) 839.
- [49] S. Masia, P.D. Calvert, W.E. Rhine, H.K. Bowen, Effect of Oxides on Binder Burnout during Ceramics Processing, *J. Mater. Sci.* 24 (1989) 1907.
- [50] P.L. Beltrame, P. Carniti, G. Audisio, F. Bertini, Catalytic Degradation of Polymers: Part II—Degradation of Polyethylene, *Polym. Degrad. Stab.* 26 (1989) 209.
- [51] J. PFITZNER, Poiseuille and His Law, *Anaesthesia* 31 (1976) 273.
- [52] S. Bhandari, C. Maniere, F. Sedona, E. De Bona, V.M. Sglavo, P. Colombo, L. Fambri, M. Biesuz, G. Franchin, Ultra-Rapid Debinding and Sintering of Additively Manufactured Ceramics by Ultrafast High-Temperature Sintering, *J. Eur. Ceram. Soc.* (2023).
- [53] H. Li, Y. Liu, Y. Liu, Q. Zeng, K. Hu, Z.L.-J. of A., and undefined, Effect of Sintering Temperature in Argon Atmosphere on Microstructure and Properties of 3D Printed Alumina Ceramic Cores, in: SpringerH. Li, Y. Liu, Y. Liu, Q. Zeng, K. Hu, Z. Lu (Eds.), *J. LiangJournal Adv. Ceram.*, 2020, Springer, 2020.
- [54] Y. Liu, Y. Liu, W. She, W. Li, Y. Cao, J. Wang, Influence of Sintering Temperature on the Thermal Conductivity of Digital Light Processing 3D-Printed Ytria-Stabilized Zirconia Ceramic, *Ceram. Int.* 49 (2023) 27514.
- [55] E. Sani, L. Mercatelli, M. Meucci, A. Balbo, L. Silvestroni, D. Sciti, Compositional Dependence of Optical Properties of Zirconium, Hafnium and Tantalum Carbides for Solar Absorber Applications, *Sol. Energy* 131 (2016) 199.
- [56] H. Kim, A. Renteria-Marquez, M.D. Islam, L.A. Chavez, C.A. Garcia Rosales, M. A. Ahsan, T.L.B. Tseng, N.D. Love, Y. Lin, Fabrication of Bulk Piezoelectric and Dielectric BaTiO<sub>3</sub> Ceramics Using Paste Extrusion 3D Printing Technique, *J. Am. Ceram. Soc.* 102 (2019) 3685.
- [57] K.W. Kirby, B.A. Wechsler, *Phase Relations in the Barium Titanate—Titanium Oxide System*, *J. Am. Ceram. Soc.* 74 (1991) 1841.
- [58] H.Y. Lee, J.S. Kim, N.M. Hwang, D.Y. Kim, Effect of Sintering Temperature on the Secondary Abnormal Grain Growth of BaTiO<sub>3</sub>, *J. Eur. Ceram. Soc.* 20 (2000) 731.
- [59] X. Sun, M. Mazur, C.T. Cheng, A Review of Void Reduction Strategies in Material Extrusion-Based Additive Manufacturing, *Addit. Manuf.* 67 (2023) 103463.
- [60] L. Lemos Da Silva, et al., Uncovering the Symmetry of the Induced Ferroelectric Phase Transformation in Polycrystalline Barium Titanate, *J. Appl. Phys.* 130 (2021).
- [61] G. Picht, N.H. Khansur, K.G. Webber, H. Kungl, M.J. Hoffmann, M. Hinterstein, Grain Size Effects in Donor Doped Lead Zirconate Titanate Ceramics, *J. Appl. Phys.* 128 (2020) 214105.
- [62] D.V. On, L.D. Vuong, T. Van Chuong, D.A. Quang, H. Van Tuyen, V.T. Tung, Influence of Sintering Behavior on the Microstructure and Electrical Properties of BaTiO<sub>3</sub> Lead-Free Ceramics from Hydrothermal Synthesized Precursor Nanoparticles, <https://doi.org/10.1142/S20101135x21500144.11> (2021) 2150014.
- [63] T. Mei, Q. Dai, W. Zheng, T. Chen, Strain Properties and Piezoelectric Constant of Lead-Free Barium Titanate Ceramics, *Mater. Res. Express* 6 (2019) 106301.
- [64] Z. Chen, et al., 3D Printing of Piezoelectric Element for Energy Focusing and Ultrasonic Sensing, *Nano Energy* 27 (2016) 78.
- [65] C.L. Liu, Q. Du, C. Zhang, J.M. Wu, G. Zhang, Y.S. Shi, Fabrication and Properties of BaTiO<sub>3</sub> Ceramics via Digital Light Processing for Piezoelectric Energy Harvesters, *Addit. Manuf.* 56 (2022) 102940.